Economic Geology, v. 106, pp. 261–288

U-Pb and ^{40}Ar-^{39}Ar Geochronology and Isotopic Constraints on the Genesis of Copper-Gold–Bearing Iron Oxide Deposits in the Hasançelebi District, Eastern Turkey

İlkay Kuşcu,[1,†] Erkan Yilmazer,[2] Nilgün Güleç,[2] Selda Bayir,[3] Gökhan Demirela,[4] Gonca Gençalioğlu Kuşcu,[1] Gülay Sezerer Kuru,[5] and Nuretdin Kaymakçi[2]

[1] *Department of Geological Engineering, Faculty of Engineering, Muğla University, TR-48000 Muğla, Turkey*

[2] *Department of Geological Engineering, Faculty of Engineering, Middle East Technical University, TR-06534 Ankara, Turkey*

[3] *Turkish Petroleum Corporation (TPAO), Sogutozu, TR-06100 Ankara, Turkey*

[4] *Department of Geological Engineering, Ankara University, TR-06100, Ankara, Turkey*

[5] *General Directorate of Mineral Research and Exploration (MTA), Çankaya TR-06800, Ankara, Turkey*

Abstract

The Hasançelebi deposit in eastern Turkey, with proven reserves of 95 million metric tons, is a copper-gold–bearing iron oxide deposit. It is chiefly hosted by rocks that underwent widespread sodic-calcic and potassic styles of alteration. In the Hasançelebi district, pervasive Na-Ca and K-Fe alteration types are overprinted by sericitization and by late alteration that occur in multiple, overprinting systems. The age of hydrothermal alteration and mineralization (ca. between 74–68 Ma) overlaps with the age of alkaline magmatism in the Hasançelebi district. Crystallization and cooling of alkaline magmatism is associated with hydrothermal features that spanned the duration of the district's igneous history. The $^{40}Ar/^{39}Ar$ and U-Pb geochronology of magmatism indicate that the hydrothermal system was synchronous with diabase and syenite and/or microsyenite porphyry intrusions and consisted of several discrete phases of Na-Ca and K-Fe alteration. The oldest alteration (phase 1) formed at ca 74.4 to 74.3 Ma; it is spatially and temporally associated with the emplacement of diabase dikes and contains scapolite and phlogopite. The next younger alteration (phase 2) formed at about 71.3 Ma and is spatially and temporally associated with syenite porphyry and microsyenite porphyry intrusions. It consists of scapolite , garnet, pyroxene, and actinolite that are superimposed on the first alteration phase. The next alteration assemblage (phase 3) formed at about 68.6 Ma and consists of phlogopite 2 and magnetite mineralization. Still later alteration (phase 4) overprints phases 1, 2, and 3 and consists of sericite-quartz, chalcopyrite, hematite, calcite, fluorite, and barite.

Oxygen ($\delta^{18}O$) and hydrogen (δD) isotope analyses were carried out on phlogopite, sericite, barite, calcite, fluorite, and quartz representing the mineral assemblage formed during phases 1 and 4 of the hydrothermal alteration. The calculated $\delta^{18}O_{(H_2O)}$ and $\delta D_{(H_2O)}$ composition of the fluids that formed preore K-Fe alteration and postore alteration of phase 4 range between 15.1 to 8.5 and –124 to –85.6 per mil, respectively, and partially overlap the range for traditional magmatic waters. Oxygen and H isotope compositions from alteration minerals highlight two major points: Na-Ca and K-Fe alteration assemblages are likely derived from high-temperature primary magmatic fluids, and late sericitization is likely derived from fluids exsolved from cooling alkaline plutons during hydrothermal fracturing and consequent degassing at moderate temperatures. The initial ε_{Ndi} values of the alteration zones range from –2.02 to –2.08, close to the calculated ε_{Nd} value of associated syenite porphyry at the time of alteration ($\varepsilon_{Nd\,(68.64Ma;}$ –1.9). Nd-Sr isotope compositions combined with ^{40}Ar-^{39}Ar and U-Pb geochronology of the associated alteration suggest that the fluids were sourced from coeval diabase dikes and syenite porphyry and/or microsyenite porphyry intrusions. The rare earth element characteristics, ^{40}Ar-^{39}Ar and U-Pb geochronology of alteration and fresh magmatic rocks, $\delta^{18}O$, δD, Nd, and Sr isotope systematics together suggest that the fluids responsible for the high- to moderate-temperature assemblages are largely derived from the coeval alkaline igneous rocks (diabase and microsyenite porphyry dikes) that intrudes the sedimentary-volcanosedimentary basin.

Introduction

Iron oxide-copper-gold (IOCG) deposits are a relatively recently recognized class of deposits and are invariably associated with very large volumes of hydrothermally altered rocks (10 to over 100 km^3). The description of general characteristics was first published by Hitzman et al. (1992), based largely on studies of Olympic Dam and prospects in the Stuart Shelf (Australia), the Kiruna district (Sweden), the southeast Missouri iron district (United States) and the Wernecke Breccias (Canada). The IOCG-type deposits globally incorporate copper (±gold ±uranium) deposits of Archean to Tertiary age that are linked primarily by the presence of abundant Ti-poor (<2 wt % TiO_2) magnetite and/or hematite and extensive alteration, particularly Fe, Na, and K metasomatism (Hitzman et al., 1992; Hitzman, 2000; Sillitoe, 2003; Williams et al., 2005) overprinted by hydrolytic alteration. Williams et al. (2005) rationalized the definition and proposed as criteria the presence of Cu with or without Au as an economic metal, hydrothermal vein, breccia and/or replacement ore styles, characteristically in specific structural sites, abundant magnetite and/or hematite, low Ti contents in iron oxides relative to those in most igneous rocks and the absence of clear spatial associations with igneous intrusions. Although magmatic and nonmagmatic ore-forming fluid sources were considered to be

† Corresponding author: e-mail, ikuscu@mu.edu.tr

Submitted: September 10, 2009
Accepted: November 12, 2010

responsible for IOCG mineralization, Williams et al. (2005) did not advocate classification of the IOCG clan of deposits on the basis of these important differences. New information from Wernecke Breccia-associated IOCG prospects suggests that the spectrum of magmatic and hybrid magmatic-nonmagmatic models for IOCG deposits should be expanded to accommodate IOCG systems formed in an environment unrelated to magmatism and include those formed from nonmagmatic fluids circulated by nonmagmatic processes (Hunt et al., 2007).

The IOCG deposits share a characteristic suite of alteration types (Hitzman et al., 1992; Haynes, 2000) ranging from early Na-(Ca-Fe) alteration overprinted by high-temperature K-Fe alteration, with late-stage, low-temperature K-Fe-H-CO_2 alteration. The calcic-sodic (Na-Ca) alteration zones are regional in scale (>1 km wide) and range from a strong albitization and scapolitization (±clinopyroxene, titanite), with calc-silicate (clinopyroxene, amphibole, garnet). The Na-Ca alterations form a characteristic assemblage consisting primarily of biotite, K-feldspar, and magnetite (de Jong and Williams, 1995; Barton and Johnson, 1996; Frietsch et al., 1997; Hitzman, 2000; Williams et al., 2005). A number of IOCG deposits contain late and structurally high-level zones of hydrolytic alteration characterized by the replacement of earlier alteration assemblages by martite (hematite after magnetite), sericite, carbonate minerals, and quartz. The main ore stage is associated with K-Fe alterations in which either sericite (at Olympic Dam and Prominent Hill) or K-feldspar (most common) prevail as the potassic phase (Skirrow et al., 2002). K-feldspar-hematite veins or an alteration assemblage of hematite-sericite-chlorite carbonate ± Fe-Cu sulfides ± U, REE minerals can be observed.

The hydrothermal fluids are hypersaline, CO_2 and $CaCl_2$ rich, S poor, and not always clearly related to igneous activity (e.g., Barton and Johnson, 1996; Pollard 2001; Williams et al., 2005), although commonly occurring within magmatic rocks at shallow to mid-crustal levels within cratonic or continental margin settings, The origin of the fluids associated with IOCG deposits is controversial. There are two main hypotheses: externally sourced, where intrusions acted as heat engines that induced hydrothermal circulation of surrounding formation waters toward the magmatic rocks (Barton and Johnson, 1996); or magmatic, where the granitoids themselves acted as the source of both the metals and fluids responsible for alteration (Hildebrand, 1986; Perring et al., 2000; Pollard 2001, 2006; Sillitoe, 2003). These hypotheses have significantly different implications for the interpretation of fluid-rock interactions in the alteration systems and for the genesis of the associated ore deposits. In the first hypothesis, the introduction of Na and Ca during sodic (calcic) alteration is generally attributed to exchange reactions between feldspar and fluid when basinal brines or externally driven fluids are heated by a magmatic heat source, or interaction of hot fluids with evaporitic sequences resulting in the addition of Na, Ca, and Cl to later alteration (Dilles and Einaudi, 1992; Barton and Johnson, 1996). The second hypothesis suggests that the alteration results from unmixing of H_2O-CO_2-NaCl-$CaCl_2$-KCl fluids released from a magma (Pollard, 2001, 2006; Sillitoe, 2003). The latter does not rule out the presence of evaporitic rocks and/or heating of externally derived fluids for the introduction of Na, Ca, K, and Cl into the hydrothermal system, as these may also contribute to alteration (Carten, 1986; Barton and Johnson, 1996). Generally, mineralogical, geochemical (Mark et al., 2006) and fluid inclusion microthermometry combined with stable isotopes of O, H, and S have been used to assess the genesis and sources of fluids in alteration and mineralization (Niiranen et al., 2007). Unfortunately, these techniques can be equivocal in identifying sources when multiple hydrothermal fluids may be involved as they can reflect a mixed isotopic signature (Haynes et al., 1995). Other techniques that have been useful in understanding the origins of the fluids include geochronology, trace element, and radiogenic isotope analysis of host rocks and hydrothermal alteration and/or mineralization in IOCG deposits (Campbell et al., 1998; Kendrick et al., 2006; Meyer et al., 2006). For many systems, there is a lack of precise age constraints for magmatism and hydrothermal alteration and/or mineralization. Radiogenic and stable isotope studies of hydrothermally altered rocks and host rocks can provide information on the source of hydrothermal fluids (Johnson and McCulloch, 1995; Campbell et al., 1998; Skirrow, 1999; Gleason et al., 2000; Mark et al., 2004a, b; Chiaradia et al., 2006; Monteiro et al., 2006; Skirrow et al., 2007). It is likely that during fluid generation and migration, rare earth elements (REE), Nd, Sr, and metals were added to the ore fluids. The study of the Nd and Sr isotope compositions can therefore be used to constrain the flow path and source of causative fluids.

Iron oxide copper-gold deposits are rare in the Tethyan-Eurasian metallogenic belt. However, Kuşcu et al. (2007a) suggested that Turkey hosts several IOCG deposits which formed in postcollisional, late-orogenic extensional settings related to the subduction of the NeoTethyan oceanic plate beneath the Eurasian plate during the Late Cretaceous to Miocene. The present state of knowledge regarding the IOCG deposits in Turkey is limited, and the iron oxide deposits of the Hasançelebi, Divriği, and Şamlı regions have been recognized as IOCG mineralization by Kuşcu et al. (2002, 2005), Yılmazer et al. (2003), and Ay et al. (2004). The iron oxide deposits of the Hasançelebi district (Hasançelebi and Karakuz iron oxide deposits) have been known for years and mined mainly for magnetite and hematite. The Hasançelebi deposit, located approximately 80 km northwest of Malatya (eastern Turkey, Fig. 1), is an abandoned low-grade iron oxide deposit with proven reserves of 95 million metric tons (Mt) @ 23 percent Fe_3O_4 (Yüce et al., 2005). The deposit is chiefly hosted by Late Cretaceous alkaline magmatic rocks that underwent pervasive sodic-calcic alteration overprinted by potassic and late hydrolytic alterations (Kuşcu et al., 2007b, c). The nature and genesis of voluminous sodic (-calcic) and potassic alteration in the Hasançelebi district remains unclear. Pilz (1937) suggested a Kiruna-type genesis, whereas İzdar and Ünlü (1985) favored a contact-pneumatolitic model. In contrast, Stendal et al. (1995), Ünlü et al. (1995), and Marschik et al. (2008) suggested that the iron oxide mineralization formed as a result of leaching and redistribution of the iron from the ophiolitic rocks during pervasive scapolitization by later hydrothermal events related to syenite intrusion. Uçurum et al. (1996) favor an orthomagmatic genetic model for the iron ores at Hasançelebi and Karakuz. Recently, Kuşcu et al. (2002, 2005, 2007b), Yılmazer

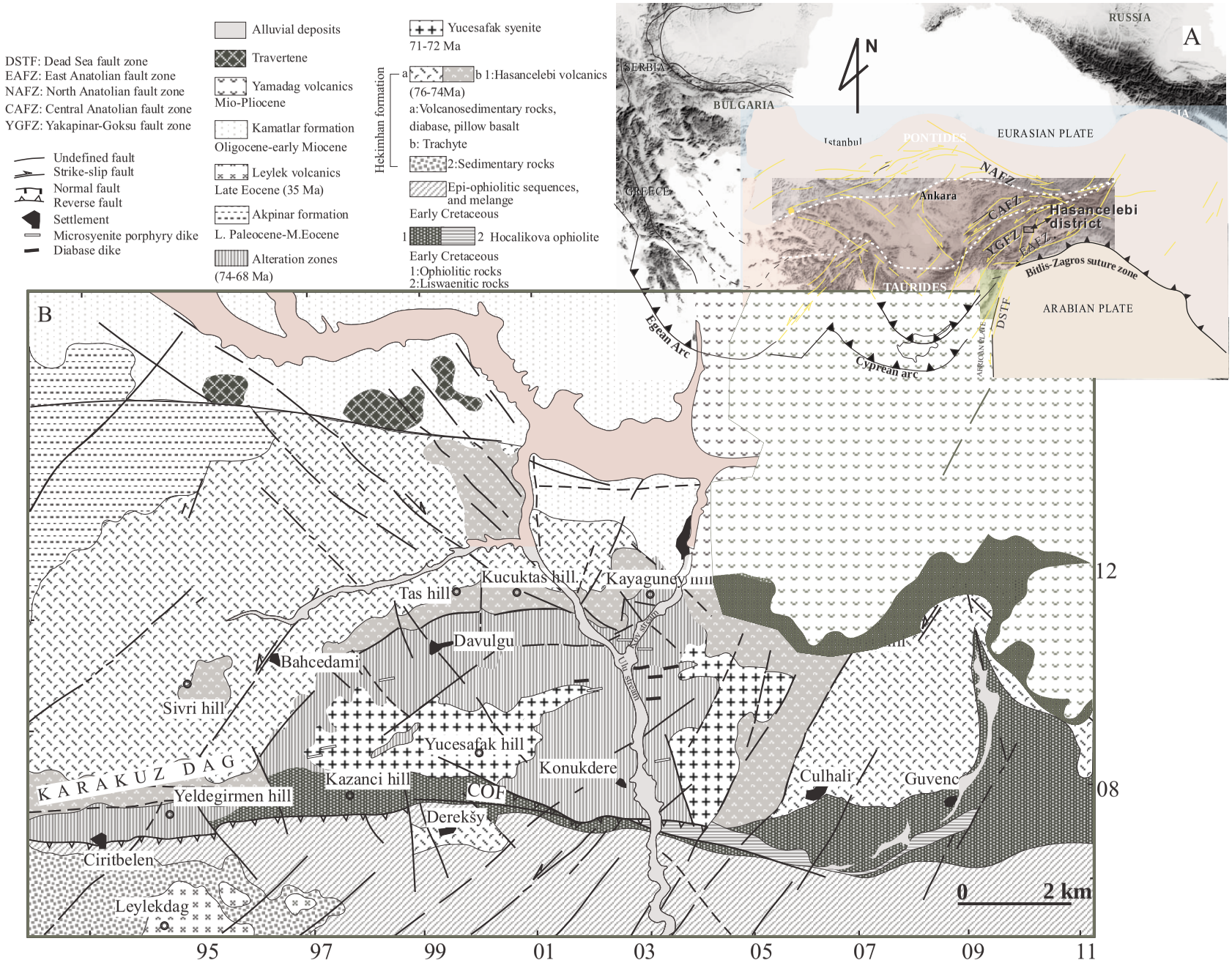

FIG. 1. A. Major tectonic units of Turkey and present-day regional setting of the Hasançelebi district. B. Simplified geologic map showing the main rock types within the Hasançelebi district (modified from Kuşcu et al., 2007c).

et al. (2003), Ay et al. (2004), and Sezerer-Kuru et al. (2006) advocated a hydrothermal origin for the mineralization.

In this paper, we present detailed field characteristics and temporal and spatial associations of different mineral assemblages for regional-scale Na-Ca and K-Fe alteration as well as new geochronological and radiogenic and stable isotope data from hydrothermal alteration zones and associated fresh magmatic rocks. The aim of the study is to investigate the possible sources and genesis of the fluids in the Hasançelebi iron oxide deposit.

Methods and Analytical Procedures

The mapping of the entire district was carried out at 1:25,000 scale; and the alteration zones were mapped on a scale at 1:5,000 scale. The mineral compositions within the alteration were determined from the optical properties of the minerals.

Geochemical analyses for REE and radiogenic isotopes of Nd and Sr were carried out at Pacific Centre for Isotopic and Geochemical Research, University of British Columbia (Canada) using inductively coupled plasma mass spectrometry (ICP-MS), after HF-$HClO_4$ digestion and lithium metaborate-sodium perborate fusion. The details of sample preparation and methodologies are given in Pretorius et al. (2006) and Weis et al. (2007). The results are presented in Table 1. Whole-rock analyses for major and trace elements were carried out at Activation Laboratories (Canada) using standard wavelength dispersive X-ray fluorescence spectrometry (XRF) from pressed powder pellets. As a routine analytical procedure, the samples are crushed to a nominal minus 10 mesh (1.7 mm), mechanically split (riffle) to obtain a representative sample and then pulverized to at least 95 percent minus 150 mesh (106 μm) using tungsten carbide plates. Sand cleaner is used between each sample to minimize the contamination.

^{40}Ar-^{39}Ar geochronology was carried out on hornblende, biotite, K-feldspar, and phlogopite separates from the fresh magmatic rock, and alteration zones. The samples were crushed, washed in deionized water, dried at room temperature, and sieved to obtain the size fraction between 0.25 and 0.15 mm. Mineral separates in an irradiation capsule with similar-aged samples and neutron flux monitors (Fish Canyon Tuff sanidine (28.02 ± 0.16 Ma), Renne et al., 1998) were irradiated at the McMaster Nuclear Reactor in Hamilton, Ontario, The samples were analyzed at Pacific Centre for Isotopic and Geochemical Research (the laser-equipped noble gas mass spectrometer—Micromass VG 5400). All measurements were corrected for total system blank, mass spectrometer sensitivity, mass discrimination, radioactive decay during and subsequent to irradiation, as well as interfering Ar from atmospheric contamination and the irradiation of Ca, Cl, and K (isotope production ratios $(^{40}Ar/^{39}Ar)_K$ = 0.0302 ± 0.00006, $(^{37}Ar/^{39}Ar)_{Ca}$ = 1416.4 ± 0.5, $(^{36}Ar/^{39}Ar)_{Ca}$ = 0.3952 ± 0.0004, Ca/K = 1.83 ± 0.01($^{37}Ar_{Ca}/^{39}Ar_K$). The plateau and correlation ages were calculated using Isoplot version 3.09 (Ludwig, 2003). Errors are quoted at the 2σ (95% confidence) level and are propagated from all sources except mass spectrometer sensitivity and age of the flux monitor (App. 1A).

The U-Pb age geochronology was carried out on zircon separates by laser ablation ICP-MS techniques at Pacific Centre for Isotopic and Geochemical Research (New Wave 213 nm Nd-YAG laser coupled to a Thermo Finnigan Element2 high-resolution ICP-MS). Ablation takes place within a New Wave "Supercell" ablation chamber which is designed to achieve very high efficiency entrainment of aerosols into the carrier gas. Helium is used as the carrier gas for all experiments and gas flow rates, together with other parameters such as torch position, are optimized prior to beginning a series of analyses. A 30-μm spot with 60 percent laser power was used. Line scans rather than spot analyses were employed in order to minimize elemental fractionation during the analyses (Košler et al., 2008). The zircons are separated from their host rocks using conventional mineral separation methods and sectioned in an epoxy grain mount along with grains of internationally accepted standard zircon and brought to a very high polish. The grains were examined using a stage-mounted cathodoluminescence imaging set-up that makes it possible to detect the presence of altered zones or inherited cores within the zircon. The highest quality portions of each grain, free of alteration, inclusions, or cores were selected for analysis. Each analysis consists of a 7-s background measurement (laser off) followed by a ~28-s data acquisition period with the laser firing. A typical analytical session consists of four analyses of the standard zircon, followed by four analyses of unknown zircons, two standard analyses, four unknown analyses, etc., and finally four standard analyses. Data are reduced using the GLITTER software package developed by the GEMOC group at Macquarie University, which subtracts background measurements, propagates analytical errors and calculates isotopic ratios and ages (App. 1B). Final interpretation and plotting of the analytical results employs ISOPLOT software (Ludwig, 2003).

Stable isotope ($\delta^{18}O$ and δD) analyses were carried out on phlogopite, sericite, calcite, barite, fluorite, and quartz, and these were analyzed at the Stable Isotope laboratories in the Geochemical Research Center of the Turkish Petroleum Corporation (Ankara, Turkey), using GV Instruments Isoprime EA-IRMS. Mineral separates were handpicked from crushed rocks. Oxygen and hydrogen isotope analyses were performed at the same laboratory. Two runs of analyses were performed on each separate to ensure good agreement of the data. Oxygen was extracted from the mineral separates using glassy carbon chips and NiC infilled reactor at 1,200°C. Hydrogen was extracted from the separates using a glassy carbon chips reactor at 1,200°C. The extracted O and H were analyzed on a GV Instruments Isoprime EA-IRMS. Oxygen ($\delta^{18}O$) and hydrogen (δD) isotope values are reported in the standard per mil notation (‰) relative to Vienna Standard Mean Ocean Water (VSMOW) as defined by Craig (1961) using the NBS-19 standard for ^{18}O ($\delta^{18}O_{VSMOW}$ = 29.32‰) and the Pollen standard for D (δD_{VSMOW} = –156.23‰; National Institute of Standards and Technology, PEF polyethylene fFoil standard). The results of standard analyses were calibrated against international standards and are within 95 percent precision. The results are mean values obtained from individual runs of analyses.

Geologic Setting

The Hasançelebi district is part of the polymetallic Baskil-Divriği province (Fig. 1; Kuşcu et al., 2007b) hosting porphyry Cu-Au, Cu-Mo-F, IOCG, epithermal Au-Cu skarn-Fe

TABLE 1. Representative Geochemical Analyses of Selected Samples from the Magmatic Rocks and Associated Alteration in the Hasançelebi Region

	Syenitic rocks						Diabase dikes				Trachytic rocks				Synore K-Fe alteration	
Sample	318	321	326	Y-2	Y-66	Y103	323	325	Y-11	Y-23	331	H3	Y-21	Y68	327(sy)	329(sy)
SiO_2	58.10	61.15	59.23	67.23	62.01	62.22	47.17	54.59	45.51	42.26	45.64	62.47	42.26	55.77	50.50	41.73
TiO_2	1.32	1.07	0.52	0.50	0.52	0.51	1.83	1.99	1.50	0.77	1.07	0.63	1.11	1.10	0.16	0.49
Al_2O_3	16.24	15.44	15.45	14.18	16.40	15.61	15.34	15.93	16.37	17.09	16.20	17.74	17.09	18.79	16.27	12.47
Fe_2O_3	3.90	1.48	1.35	1.51	2.20	2.70	7.02	13.65	10.18	8.26	11.32	1.35	8.26	1.45	7.16	16.36
MnO	0.03	0.04	0.05	0.04	0.03	0.09	0.08	0.11	0.06	0.07	0.04	0.03	0.07	0.06	0.03	0.06
MgO	2.33	1.44	0.15	0.10	0.30	0.33	4.80	2.70	6.22	6.10	6.26	1.33	6.10	0.78	3.16	7.42
CaO	4.98	5.08	7.58	4.28	3.55	3.04	11.49	4.19	11.19	7.87	7.49	2.12	7.87	5.81	6.32	8.84
Na_2O	3.40	2.90	8.50	8.07	3.35	0.84	4.97	5.17	1.33	3.27	4.69	5.43	3.27	7.51	7.41	3.88
K_2O	6.94	8.23	0.40	0.14	8.79	10.19	1.65	3.46	3.74	4.87	2.78	6.37	4.87	2.04	2.19	1.65
P_2O_5	0.36	0.29	0.12	0.18	0.11	0.13	0.47	0.60	0.39	0.47	0.42	0.03	0.47	0.84	0.07	0.48
LOI	2.00	2.29	5.87	3.48	2.83	3.92	4.45	1.68	3.89	8.85	3.65	1.92	8.85	4.65	5.72	4.82
Total	99.95	99.32	99.23	99.70	100.08	99.58	99.22	99.57	99.98	99.89	99.43	99.42	99.89	98.81	98.94	98.72
Ba	2940.00	3598.00	122.00	429.00	974.00	1300.00	1219.00	1045.00	962.00	2240.00	605.00	4590.00	1460.00	742.00	1018.00	496.00
Rb	99.80	48.80	3.94	n.d	95.00	259.00	64.00	105.00	137.00	131.00	144.00	89.00	303.00	55.00	61.50	267.00
Sr	326.00	273.00	175.00	72.00	161.00	111.00	573.00	242.00	414.00	96.00	439.00	400.00	483.00	672.00	283.00	240.00
Cs	2.34	0.29	0.13	0.50	n.d	1.40	0.98	1.71	0.90	6.60	5.55	52.00	n.d	21.10	7.30	
Li	326.00	15.80	23.80	n.d	n.d	n.d	48.00	n.d	n.d	35.00	n.d	n.d	n.d	11.90	64.20	
Ga	21.10	24.00	26.70	22.00	22.00	22.00	18.70	20.80	16.00	27.00	17.80	23.00	18.00	16.00	16.10	20.40
Ta	2.50	2.86	6.30	2.50	3.80	3.70	1.86	2.30	1.00	1.90	1.24	4.80	1.70	1.70	0.26	2.55
Nb	40.80	44.00	98.00	32.00	52.00	48.00	25.60	34.70	16.00	92.00	17.10	73.00	29.00	26.00	2.73	23.00
Hf	8.90	8.80	17.30	7.20	10.90	9.60	3.60	6.70	4.00	3.80	4.54	8.60	3.70	3.50	6.88	5.77
Zr	341.00	421.00	945.00	283.00	463.00	416.00	159.00	256.00	151.00	125.00	187.00	431.00	177.00	183.00	377.00	280.00
Ti	1.00	1.00	n.d	n.d	n.d	n.d	1.00	1.00	1.00	n.d	1.00	n.d	1.00	1.00	n.d	n.d
Y	44.30	35.00	42.00	28.00	30.00	34.00	23.00	42.30	25.00	94.00	16.30	43.00	22.00	30.00	6.50	12.30
Th	20.40	23.90	62.00	24.20	42.40	31.80	6.28	16.35	9.70	31.30	14.40	26.30	18.30	13.60	6.70	39.00
U	13.05	11.86	12.30	5.50	10.60	5.20	5.44	6.39	4.10	27.70	7.30	8.00	7.70	8.40	n.d	6.20
Cr	30.00	6.29	2.10	233.00	132.00	142.00	908.00	10.00	169.00	51.00	178.00	186.00	40.00	75.00	11.90	7.70
Ni	38.00	10.00	22.90	20.00	n.d	n.d	31.00	8.00	48.00	979.00	69.10	26.00	35.00	n.d	34.80	152.00
Co	9.60	6.29	6.70	1.00	3.00	3.00	12.60	14.80	16.00	167.00	29.70	4.00	14.00	2.00	17.30	26.70
Sc	38.00	8.50	2.10	7.00	3.00	3.00	24.00	n.d	23.00	n.d	25.00	3.00	9.00	9.00	11.90	7.22
V	113.00	42.40	23.80	33.00	15.00	25.00	214.00	175.00	158.00	299.00	209.00	18.00	125.00	71.00	79.80	138.00
Cu	21.00	5.40	16.80	21.00	50.00	n.d	9.90	21.00	117.00	139.00	47.00	26.00	28.00	12.00	27.30	16.40
Pb	14.00	9.10	2.10	5.00	n.d	n.d	4.16	10.00	15.00	3.51	n.d	n.d	n.d	2.46	2.24	
Zn	45.00	7.80	1.63	30.00	n.d	n.d	19.30	73.00	32.00	96.00	35.90	n.d	n.d	n.d	18.10	53.00
Bi	14.00	0.08	0.42	0.40	2.60	0.60	88.00	n.d	1.30	0.40	0.18	4.50	n.d	0.60	0.08	116.00
Cd	45.00	0.19	0.19	n.d	n.d	n.d	0.09	n.d	n.d	n.d	0.02	n.d		0.11	0.13	
Sn	7.00	4.90	5.10	3.00	4.00	7.00	2.06	3.00	3.00	1.00	0.71	5.00	3.00	3.00	n.d	2.10
W	8.00	0.54	2.47	10.00	2.00	3.00	1.64	4.00	4.00	2.00	1.17	1.00	2.00	3.00	0.63	0.40
Mo	20.00	0.56	0.73	8.00	5.00	5.00	1.58	4.00	2.00	2.00	0.32	6.00	n.d	3.00	2.73	1.68
La	70.20	88.00	31.00	19.90	41.40	51.20	50.00	56.10	32.30	92.00	41.00	31.40	41.20	28.70	8.90	34.00
Ce	145.50	172.00	80.00	40.80	90.20	104.00	79.00	109.50	59.10	141.00	76.00	89.70	75.80	62.50	14.60	50.00
Pr	15.55	14.40	10.80	4.81	10.00	11.30	6.50	12.55	7.11	24.20	7.40	12.10	8.69	7.83	1.34	4.20
Nd	52.50	49.00	45.00	17.80	32.80	37.80	23.30	46.60	27.70	112.00	29.20	45.00	31.30	30.10	5.10	14.40
Sm	9.17	8.10	8.96	3.70	5.50	6.50	4.30	9.27	5.50	27.70	4.76	8.70	5.40	5.50	0.98	2.28
Eu	2.64	2.51	1.19	0.72	1.09	1.39	1.19	3.26	2.71	8.56	1.19	2.22	1.38	2.11	0.33	0.53
Gd	9.03	6.60	7.40	3.70	4.50	5.80	4.36	9.63	4.80	24.30	2.94	8.00	4.30	5.80	0.92	2.06
Tb	1.30	0.99	1.24	0.60	0.80	0.90	0.63	1.39	0.80	3.60	0.51	1.30	0.70	0.80	0.14	0.29
Dy	7.20	6.20	8.20	3.90	4.40	5.20	3.93	7.81	4.20	17.60	3.03	6.90	3.60	4.40	1.00	1.80
Ho	1.50	1.27	1.63	0.80	0.90	1.10	0.83	1.63	0.80	3.20	0.59	1.50	0.70	0.90	0.23	0.38
Er	4.54	3.73	4.90	2.50	3.00	3.40	2.39	4.72	2.40	8.90	1.69	4.40	2.20	2.60	0.78	1.09
Tm	0.62	0.54	0.71	0.39	0.50	0.54	0.33	0.66	0.33	1.27	0.23	0.69	0.32	0.37	0.14	0.17
Yb	4.38	3.74	4.80	2.60	3.40	3.50	2.30	4.28	2.00	7.70	1.57	4.50	2.00	2.30	1.09	1.36
Lu	0.64	0.59	0.73	0.41	0.51	0.54	0.36	0.65	0.28	1.08	0.23	0.63	0.29	0.33	0.22	0.23
Nb/Ta	16.32	15.38	15.55	12,8	13.68	12.97	13.76	15.08	16.0	48.42	13.79	15.2	17.05	15.3	10.05	9.01
Zr/Hf	38.31	47.84	54.62	39.30	42.47	43.33	44.16	38.20	37.75	32.89	41.19	50.11	47.83	52.28	54.79	48.52

Notes: Major elements in wt %, trace elements in ppm, n.d = not detected, sy = syenitic rock

and Pb-Zn mineralization in the eastern Taurides (Turkey). The Baskil-Divriği province is oblique to the general northeast-trending belts of magmatic rocks. It is also oblique to the sinistral Yakapınar-Göksun fault zone and is normal to the Bitlis-Zagros suture zone (Fig. 1). The province is located to the north of the Southeastern Anatolian orogenic belt (Fig. 1), a microcontinent rifted from Gondwanaland during early Mesozoic (Şengör and Yılmaz, 1981; Robertson and Woodcock, 1982). The southeastern Anatolian orogenic belt and Tauride units were accreted to the Arabian margin by mid-Cenozoic, possibly accompanying transtensional deformation (Robertson, 1998; Stampfli, 2001). In the province, six Late

Cretaceous to Plio-Quaternary tectonomagmatic units are definedL (1) a basement of Late Cretaceous high-grade metamorphic rocks (Bitlis-Pötürge and Keban metamorphics), (2) Late Cretaceous ophiolites and ophiolitic mélange (Güneş and Guleman-İspendere ophiolites, Beyarslan and Bingöl, 2000) obducted onto the basement, (3) Late Cretaceous subduction-related magmatism (Baskil-Yüksekova arc), (4) Late Cretaceous-Miocene continental to marine sedimentary-volcanosedimentary sequences (Hekimhan basin) overlying the metamorphic and ophiolitic rocks, (5) Late Cretaceous postcollisional to late orogenic magmatic rocks emplaced into the basement and sedimentary sequences, and (6) marine sedimentary and volcanic rocks of Paleocene-Eocene age overlain by continental sedimentary and volcanic units of Miocene to Plio-Quaternary age.

The Bitlis-Pötürge and Keban metamorphic rocks consist primarily of slate, phyllite, quartzite, metapelite, calcareous schist, and marble. They represent a late Paleozoic to Mesozoic (Özgül et al., 1981) platform-type carbonate and fine-grained clastic rock succession that formed part of the Tauride platform located along the northern margin of the southerly Neotethys Ocean. These rocks were metamorphosed to greenschist facies beneath ophiolitic nappes and ophiolitic mélange (Perinçek and Kozlu, 1984; Yılmaz et al., 1987) derived from the Vardar ocean (Channel and Kozur, 1997; Stampfli et al., 1998) and then exhumed during the Late Cretaceous. The ophiolitic rocks in the Baskil-Divriği province (Guleman-İspendere ophiolites) are of suprasubduction zone-type ophiolites (Yalınız et al., 1999; Beyarslan and Bingöl, 2000; Parlak et al., 2004; Robertson et al., 2005). Late Cretaceous to Tertiary sedimentary and volcaniclastic rocks overlie the ophiolites. In the eastern Taurides, the Late Cretaceous magmatic complexes consist of sequential arc to postcollisional volcano-plutonic products and within-plate magmatic rocks which intrude the underlying deformed metasedimentary and ophiolitic rocks due to the closure of the NeoTethys ocean along the Bitlis-Zagros subduction zone (Kuşcu et al., 2010). Late Cretaceous (ca.74–69 Ma) postcollisional magmatism throughout the eastern Taurides and immediately adjoining regions are generally considered to have taken place under extensional conditions in response to retreating subduction boundaries (slab roll-back) along the Bitlis-Zagros subduction zone (Kuşcu et al., 2007a; 2010). These are represented by calc-alkaline and alkaline associations. The calc-alkaline suites are generally older, whereas the alkaline suites are younger and generally accompanied by extension-related basin formation and deposition of volcaniclastic sequences. Extension is interpreted to have been driven by slab roll-back following the collision and obduction of northerly ophiolites from the Vardar ocean (Kuşcu et al., 2010). Late Cretaceous-middle Eocene continental to marine sedimentary-volcanosedimentary sequences are found within the Hekimhan basin (Fig. 1) formed above the obducted ophiolitic nappe rooted to the Vardar ocean during that extension (Gürer and Aldanmaz, 2002; Kuşcu et al., 2010). The basin infill within the Hekimhan basin consists of Late Cretaceous to Paleocene continental to shallow marine sedimentary rocks overlain by Paleocene to middle Eocene marine sequences (Fig. 1) and coeval alkaline extrusive and intrusive rocks (Kuşcu et al., 2007a-d). Late Cretaceous-middle Eocene sedimentary and accompanying magmatic rocks are overlain by continental clastic rocks of Oligo-Miocene age. All these rock units are overlain by a Mio-Pliocene volcanic sequence consisting of basaltic andesite, dacite, rhyolite (Yalçın et al. 1998), and tuffaceous to conglomeratic rocks.

Extensive east-west– to northeast-southwest–oriented brittle fault systems, including northeast-southwest–trending Malatya-Ovacık (Kaymakçı et al., 2006), Göksu-Sarız, Kangal-Cetinkaya, and Central Anatolian fault zones in central-eastern Anatolia appear to control the emplacement and/or exposure of the causative magmatic rocks and spatial association of sodic alteration zones (Fig. 1). These follow an oblique northeast-southwest trend from the southeastern coast of Turkey to Erzincan-Sivas as a series of northwest-and north-northeast–striking brittle faults which underwent variable sinistral strike-slip motion (Fig. 1).

Rock Units and Local Stratigraphy

The host sequence in the Hasançelebi district (Fig. 1) is composed predominantly of alkaline volcanic (both effusive and explosive) and plutonic rocks emplaced into the Hekimhan basin. The Hekimhan basin lies unconformably on the ophiolitic rocks and contains a package of sedimentary and volcanosedimentary rock units (Hekimhan formation) characterized by continental clastics (Gürer, 1992, 1996), marine sedimentary sequences intercalated with volcanic and volcanosedimentary rocks. The ophiolitic rocks, locally termed the Hocalıkova ophiolites (Gürer, 1992, 1996), represent a disrupted and incomplete ophiolite sequence. In the Hasançelebi district, they were mapped as chaotic units at the southern margin of the alteration zones extending between the Ciritbelen and Güvenç villages (Fig. 1). The ophiolites consist of gabbro, cumulate gabbro, wherlite, serpentinized pyroxenite, harzburgite, and lherzolite (Gürer, 1992; Stendal et al., 1995). They are overlain by epiophiolitic sequences and mélange consisting of chaotic mixture of serpentinite blocks, pillow lavas, polymictic conglomerate, sandstones, shales, and chert to fine-grained micritic limestones. These are cut by trachytic dikes and plugs. The ophiolitic rocks contain prominent linear ridges of quartz-carbonate-magnesite alteration (listwaenite) traceable along strike for more than 20 km along the Ciritbelen-Otmangölü fault (Fig. 2) which is a south dipping (60°–70°) reverse fault.

The Hekimhan formation consists of sedimentary, volcanosedimentary rocks and Hasançelebi volcanics. The sedimentary rocks of the Hekimhan formation (late Campanian-Maastrichtian in age; Gürer, 1992) are mostly exposed at the southwestern margin of the mapped area and is displaced by northeast-southwest–trending strike-slip to normal faults. The Hekimhan formation begins with continental basal conglomerate and sandstone and grades into shallow marine sediments (sandstone-marl-shale interbeds) at the top. This sequence is overlain by shallow marine carbonates of late Campanian-early Maastrichtian (Gürer, 1992).

The Hasançelebi volcanics and Yüceşafak syenite are the two main igneous rocks associated with sedimentary rocks of the Hekimhan formation. The mineral assemblage and textural features of the igneous rocks in the Hasançelebi district are summarized in Table 2. The Hasançelebi volcanics, exposed mainly at the eastern, western, and northern parts of

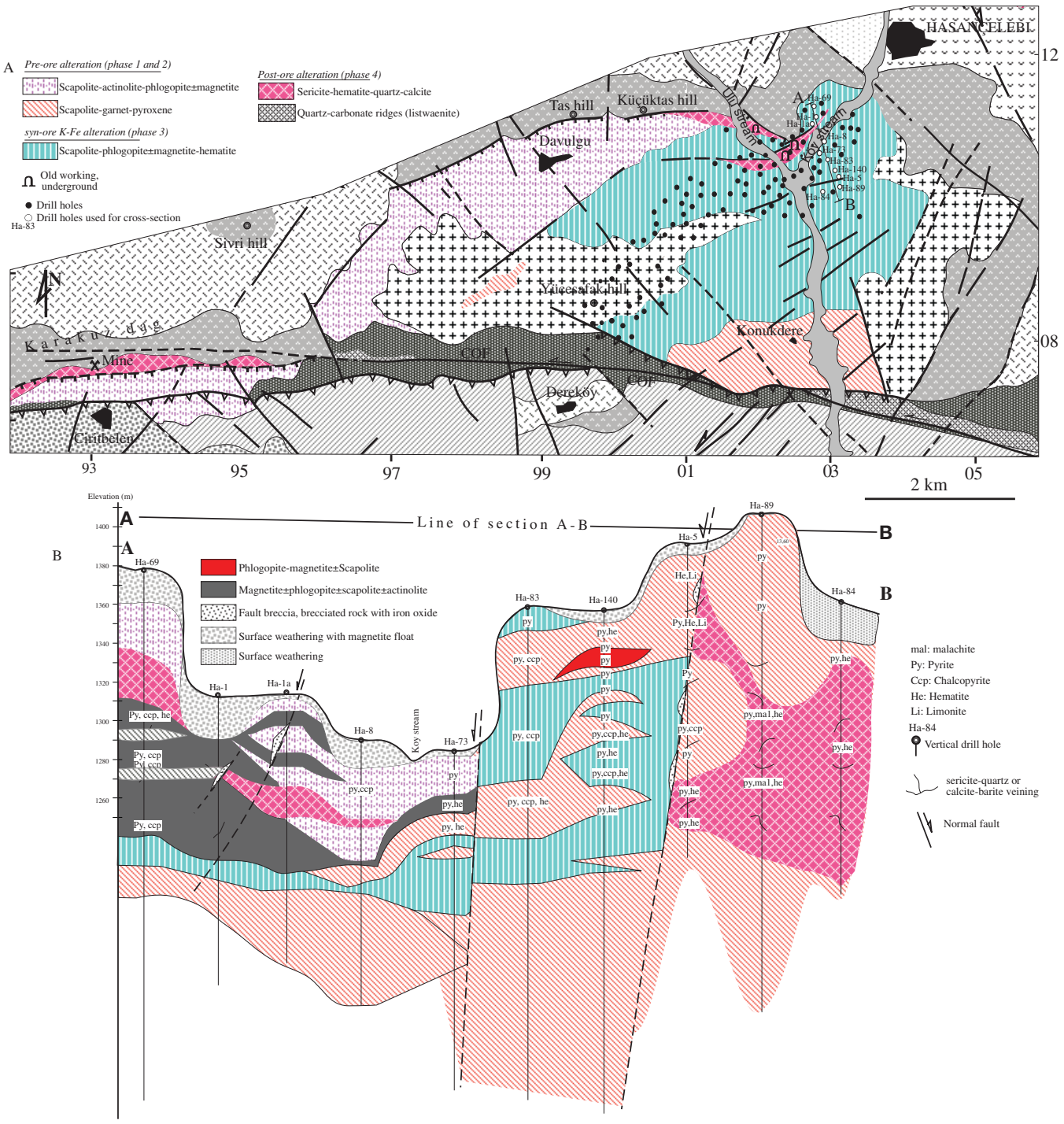

FIG. 2. A. Alteration map of the Hasançelebi district showing the main alteration zones (modified from Kuşcu at al., 2007c). B. Cross section along line A-B based on drill hole data (Kuşcu et al., 2007c).

the district, occur either as intercalations prevailing at fine-grained sedimentary facies of the Hekimhan formation or as large domes enveloping the alteration within the district (Figs. 1, 2). The Hasançelebi volcanics consist of pyroclastic rocks and lava flows, cut by diabase dikes.

The pyroclastic rocks are mainly exposed along the Ciritbelen-Otmangölü fault and at the base of the volcanic sequence, at the Taş hill, to the north of Çulhalı village. They include agglomerate, volcanic breccia, lapilli tuff, and tuff as infrequent horizons within the volcanic rocks with well-developed bedding (Gürer, 1992). Lava flows consist of trachytes, trachy-andesites (Gürer, 1992; Yılmaz et al., 1993), pillow basalts, and spilites. Trachytes and trachy-andesites consisting mainly of plagioclase (Table 2) and chloritized biotite hornblende, are

TABLE 2. Mineral Assemblage and Textural Features of the Igneous Rocks in the Hasançelebi District

Rock unit	Mineral assemblage	Shape, outline	Textural features/alteration
Trachyte	Phenocrysts:		
	Sanidine (50–30%)		Vitrophyric-trachytic
	Plagioclase (30–10%)		
	Biotite (3–15%)		
	Hornblende (3–5%)		
	Groundmass:		
	Glass and plagioclase microlites		
Spilite, pillow basalt	Plagioclase (10–20%)	Prismatic, subhedaral	
	Olivine (15–20%)	Irregular	Amygdaloidal
	Hornblende (5–10%)		
	Accessories:		
	Siderite, magnetite		Infilling
Diabase	Phenocrysts:		
	Pyroxene (augite)		Subophitic
	Hornblende		
	Plagioclase		
	Groundmass:		
	Plagicolase microliths		
Yüceşafak Syenite	Phenocrystys:		
	Plagioclase (≤20%) (An_{25-30})	Prismatic, subhedaral	Myrmekitic
	K-feldspar (≤60%) (orthoclase and microcline)	Anhedral	Perthitic, antiperthitic, antirapakivi
	Pyroxene (≤10%) (aegerine augite)		Partly converted into amphibole
	Quartz (≤5%)	Acicular	
	Accessories:		
	Zircon, apatite, titanite		Mostly fractured
Andesite, rhyodacite (Leylekdağ volcanics)	Phenocrysts:		
	Plagioclase (fine to medium grained)	Subhedral	Vitrophyric
	Hornblende		
	Pyroxene		
	Biotite (fine grained)		
	Groundmass:		
	Glass and plagioclase microlites		

exposed either as east-west–trending domes, or as flows intercalated with fine-grained sedimentary rocks. These form linear ridges at the northern parts of the mapped area along east-west–trending high-angle normal faults (Fig. 1). The trachytic rocks show local hydrofracturing and brecciation at the Karakuz dağ (Fig. 1) and at the southern flank of Taş hill (Figs. 1, 2). The pillow-structured basalts and spilites are exposed as small-scale bodies within marl-shale interbeds of the Hekimhan formation around the Küçüktaş hill, Bahçedamı village, and Dereköy (Fig. 1). The amygdules in the spilitic basalts are filled by calcite and iron oxide minerals (mostly siderite and magnetite). Diabase dikes, cutting the Hasançelebi volcanics, occur as east-west–trending (Fig. 1) and almost vertical dike systems up to 100 m long, or as sill-like intrusions within the sedimentary and volcanic rocks. The thickness of individual dikes ranges from 30 to 100 cm.

The plutonic rocks in the Hasançelebi district are syenitic in composition and occur as massive stocks and aplitic and porphyritic dikes—collectively termed Yüceşafak syenite (Gürer, 1992). Yüceşafak syenite crops out as two major discrete bodies separated by the Uludere stream (Figs. 1, 2). The ophiolites are thrust over the syenitic rocks along the east-west–trending Ciritbelen-Otmangölü fault (Fig. 1). The aplitic and porphyritic dikes are exposed randomly within the syenitic body itself mainly close to the margins of the massive stock, or cut the Hasançelebi volcanics in east-west to northeast-southwest directions, mostly parallel to or cutting the diabase dikes. They cannot be traced laterally for more than a few tens of meters. The dikes are microsyenite and microsyenite porphyry in composition (Gürer, 1992). These are also accompanied by aplitic dikes along the marginal parts of the microsyenite porphyry dikes. The syenites are medium to coarse grained and contain numerous elliptical to spherical mafic enclaves (<8 cm diam) of syenodiorite. They consist predominantly of K-feldspar, plagioclase, pyroxene, and quartz as major constituents; and titanite, coarse zircon, and acicular apatite as accessory phases (Table 2).

The Akpınar formation, unconformably overlying the former units, consists primarily of sedimentary rocks of late Paleocene to middle Eocene age (Gürer, 1992), including cross-bedded basal conglomerates and evaporitic sequences (mostly gypsum). The Akpınar formation is overlain by andesite to dacite flows, rhyodacite to dacite domes, and dacitic tuff to agglomeratic rocks, collectively termed the Leylekdağ volcanics (Gürer, 1992). The $^{40}Ar/^{39}Ar$ K-feldspar geochronology for the dacites gave an age of 34.4 Ma (Kuşcu et al., 2007c).

The Olio-Miocene–aged continental sedimentary rocks of the Kamatlar formation unconformably overly the Akpınar formation and consist of poorly bedded, unsorted coarse clastic rocks including conglomerate, sandstone, and marl-siltsone

alternations. The Kamatlar formation is overlain by the Yamadağ volcanics exposed mainly at the northeastern part of the district. The Yamadağ volcanics start with tuff and lapilli tuff at the base (Gürer, 1992) and grade into basaltic trachyandesite, olivine basalt, and andesite flows (Yalçın et al., 1998) toward the stratigraphic top.

The Hasançelebi district and surrounding areas are displaced predominantly by normal and strike-slip faults. These trend mostly in northeast-southwest to northwest-southeast and east-west directions (Figs. 1, 2). Northeast-southwest– and east-west–trending faults are almost parallel to the diabase and microsyenite porphyry dikes. The structural elements and their association with the basin evolution, magmatism, and alteration were developed under four predominant stress regimes and deformation phases (Kaymakçı et al., 2006). Each phase formed its characteristic structure or reactivated or reconfigured the preexisting structures under the new stress regime (Kaymakçı et al., 2006; Kuşcu et al., 2007c). Of these regimes, it appears that the first deformation phase (D_1; Kaymakçı et al., 2006) that resulted in a northeast-southwest–trending extensional regime and regional fault systems trending in a northeast-southwest direction has a prominent control on the formation of the Hekimhan basin, syntectonic sedimentation (Kaymakçı et al., 2006), alkaline magmatism, and alteration in the district (Kuşcu et al., 2007c). This regime was active between the Late Cretaceous and late Eocene (Kaymakçı et al., 2006).

Mineralization and Structural Control

The Hasançelebi deposit consists chiefly of magnetite hosted mainly by (late) phlogopite-altered syenitic rocks and (late) phlogopite-actinolite–altered trachytic rocks (Fig. 2B). The magnetite is often altered into hematite along the shear zones during sericitization. Drill hole data revealed that the iron oxide bodies are mainly subhorizontal to horizontal and occur as lensoidal and pocketlike masses (Fig. 2B) and contain copper (0.8–2.75%) gold (0.04–2 g/t), and nickel (2 ppm to 1.9%). Uneconomic copper mineralization is related either to chalcopyrite disseminations within sericite-quartz-calcite veins or mostly to malachite-goethite stained quartz-calcite-pyrite veins and veinlets. Hematite-Cu-Au± mineralization is hosted mainly by trachytic and by syenitic rocks.

The alteration and iron oxide-(Cu ± Au) mineralization in the Hasançelebi district is localized within east-west–, northeast-southwest– to east-northeast–west-southwest–trending structures (Kuşcu et al., 2007c). The alteration is predominantly sodic-calcic overprinted by potassic and hydrolytic alterations. The spatial and temporal relationships between the alteration mineral assemblages in the district reflect five overlapping hydrothermal phases. For the most part, the hydrothermal assemblages of early alteration phases are largely distributed along east-west–trending structures, which are also loci for emplacement of diabase dikes. On the other hand, the assemblages of later alteration phases are largely preserved as pervasive and massive replacement features focused in the N 60-70 E–trending fractures. These are conformable with the structures formed during the first deformation phase (D_1; Kaymakçı et al., 2006). This indicates that magmatism and alteration were intermittently active within a protracted series of tectonic and hydrothermal events mainly during the Late Cretaceous (Kaymakçı et al., 2006; Kuşcu et al., 2007c).

Geochemistry of Igneous Rocks

The nomenclature of igneous host rocks in the Hasançelebi district is based on the total alkali-silica diagram given in Figure 3A. As can be seen from this figure the rocks are classified as basalt, trachyte and/or syenite, trachy-andesite and/or syenodiorite. Since total alkali and silica contents are highly variable in hydrothermal environments, we also employed the Winchester and Floyd (1977) diagram using the relatively immobile trace elements in Figure 3B. The same nomenclature applies also in Figure 3B. Both Figure 3A and B reveal that the igneous rocks in the district are alkaline in nature. The alkalinity of these rocks is also addressed in a recent study by İlbeyli and Özgenç (2008). The rocks are generally enriched in REE relative to chondrites (Fig. 3C) and in low field strength (LFS) compared to high field strength (HFS) elements (Fig. 3D), with prominent negative anomalies in K and Ti. Nb shows a moderate to weak negative anomaly, whereas Rb and Th display positive anomalies. All samples are characterized by significant flattening of HREE patterns relative to the LREE and show negative Eu anomalies in syenitic and trachytic rocks (Fig. 3C). The syenitic rocks are more enriched in HREE compared to trachytic and diabasic rocks and exhibit typical mantle ratios (Nb/Ta = 16.3–12.8 and Zr/Hf = 54.6–38.3). In general, the igneous rocks and associated alteration-mineralizations display similar REE patterns, and the rocks from the alteration zones show depletion in REE relative to the igneous host rocks (see inset in Fig. 3C). The igneous rocks in the district plot as within-plate granitoids to syncollisional granite (syn-COLG) settings based on their Nb, Y , Yb, and Ta contents (Fig. 3E, F) as also suggested by Yılmaz et al. (1993) and İlbeyli and Özgenç (2008). They have high Th/Yb and Ta/Yb ratios (Fig. 3G), suggesting the effects of both subduction and within-plate enrichment processes in the source region of the magmatism. Nb/Ta and Zr/Hf ratios of the syenitic rocks are suggesting a metasomatized mantle source (İlbeyli and Özgenç, 2008). The rocks have intermediate Yb/Ta and Y/Nb ratios, and almost all samples plot in the ocean island basalt (OIB) and arc granite fields in Figure 3H (Yb/Ta vs. Y/Nb plot) along a linear trend. Further, the samples plot in the subfield of Jurassic White Mountain A-type granitoids consisting mainly of syenitic, granitic, and mafic rocks generated in an extension-related setting (Fig. 3H; Best and Christiansen, 2001). However, they also reflect an arc-volcanic affinity (Fig. 3I) and lamprophyric association (Fig. 3J).

Hydrothermal Alteration, Paragenesis, and Mineralization

Hydrothermal activity was widespread in the district, and alteration is exposed within an ellipsoidal area conformable mainly to east-west– to N 70-80 E–trending syenitic intrusion (Fig. 2). The IOCG mineralization and alteration is hosted by the alkaline igneous rocks and Late Cretaceous-Paleocene sedimentary-volcano-sedimentary sequence. The hydrothermal alteration is absent in the sedimentary rocks and limited in the diabases, whereas it is pervasive in the trachytic and syenitic rocks. The trachytic and syenitic rocks of the Hasançelebi district have been affected by extensive scapolite

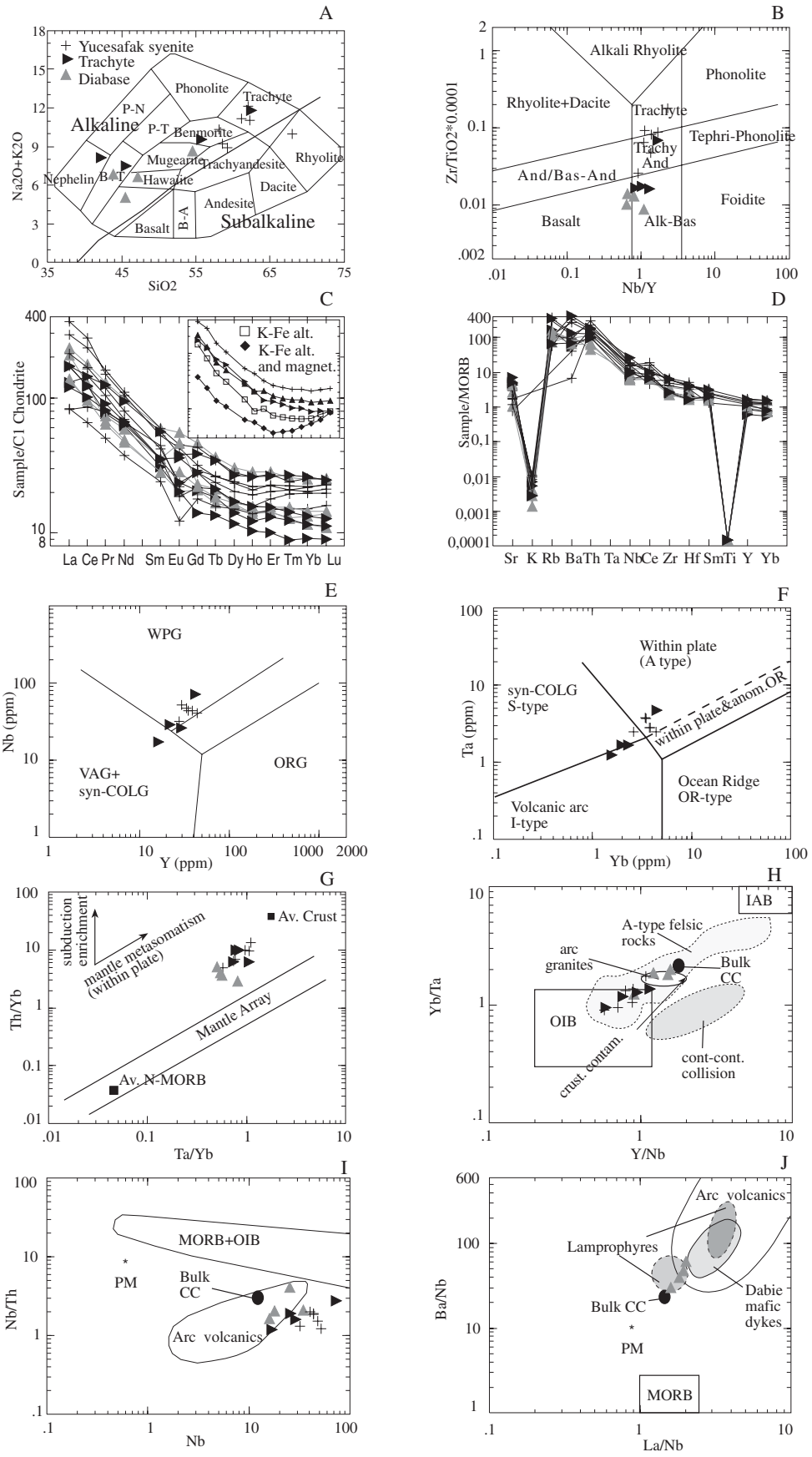

FIG. 3. A. Total alkalis vs. silica (TAS) plot of Cox et al. (1979). B. Modified Zr/TiO_2-Nb/Y plot (Pearce, 1996) of Winchester and Floyd (1977). C. Rock and/or chondrite-normalized REE. D. Rock and/or MORB-normalized spidergrams. E. Nb-Y and F. Ta-Yb diagrams of Pearce et al. (1984). G. Th/Yb vs. Ta/Yb diagram (Pearce, 1983), showing the effect of mantle metasomatism. H. Yb/Ta-Y/Nb diagram (Whalen et al., 1987; Best and Christiansen, 2001), showing the effect of crustal contamination and within plate signature. I. Nb/Th-Nb diagram showing arc volcanics, ocean island basalt (OIB), continental crust (CC), primitive mantle (PM) (data after Schimidberger and Hegner, 1999). J. Ba/Nb-La/Nb diagram. Data for MORB, PM, and Dabie mafic dikes are from Le Roux (1986), Sun and McDonough (1989), and Wang et al. (2005), respectively.

(Na, Na-Ca) overprinted by K-Fe alteration covering an area of about 70 km² (Fig. 2). Drilling in the district has shown that the observed thickness of the alteration can reach up to 400 m (Fig. 2). Scapolite, garnet, and actinolite are the major constituents in Na and Na-Ca alteration. Other minerals in Na-Ca alteration include pyroxene, titanite, and apatite as minor constituents. Dark-colored, coarse- to fine-grained phlogopite and magnetite with minor K-feldspar dominate in K-Fe alteration. These are overprinted by sericite-quartz-hematite-carbonate alteration. The most prominent alteration, composed of pervasive scapolite-garnet-pyroxene and scapolite-phlogopite ± magnetite assemblages (Na, Na-Ca and K-Fe alteration), occurs mainly within the syenitic rocks (syenite, syenite porphyry, and microsyenite porphyry dikes). The alteration is so pervasive that the original rock texture is almost obliterated and the syenite and syenite porphyry are converted completely into massive scapolite-rich rock on both sides of the Ulu stream (Fig. 2). The intensity of alteration increases with the frequency of syenite porphyry and microsyenite porphyry dikes, and the alteration minerals (scapolite and phlogopite) become coarser between the individual dikes. The alteration within the trachytic rocks is commonly localized along syenite-trachyte boundaries (Fig. 2), and these contain an assemblage of scapolite-actinolite-phlogopite ± magnetite.

Figure 2 shows the spatial association of the predominant alteration assemblages in four distinct zones from the Ciritbelen-Otmangölü fault at the south to Küçüktaş hill to the north. These zones are (1) scapolite-garnet-pyroxene hosted by syenitic rocks immediately north of ophiolites, (2) scapolite-phlogopite ± magnetite-hematite hosted by syenitic and trachytic to diabasic rocks, (3) scapolite-actinolite-phlogopite ± magnetite hosted by trachytic rocks, and (4) sericite-hematite-quartz-calcite hosted by syenitic and trachytic rocks. The iron oxide mineralization (magnetite and hematite) are hosted by phlogopite-bearing, and sericite, calcite-bearing alteration zones, respectively.

The nature and distribution of the alteration types and spatial and temporal relationships between the alteration minerals and igneous rocks in the district reflects five overlapping hydrothermal phases (Fig. 4) that were associated with individual intrusions of diabase and syenite, syenite porphyry and microsyenitic dikes along the major structural conduits (Kuşcu et al., 2005, 2007c; Table 3). The earlier findings of

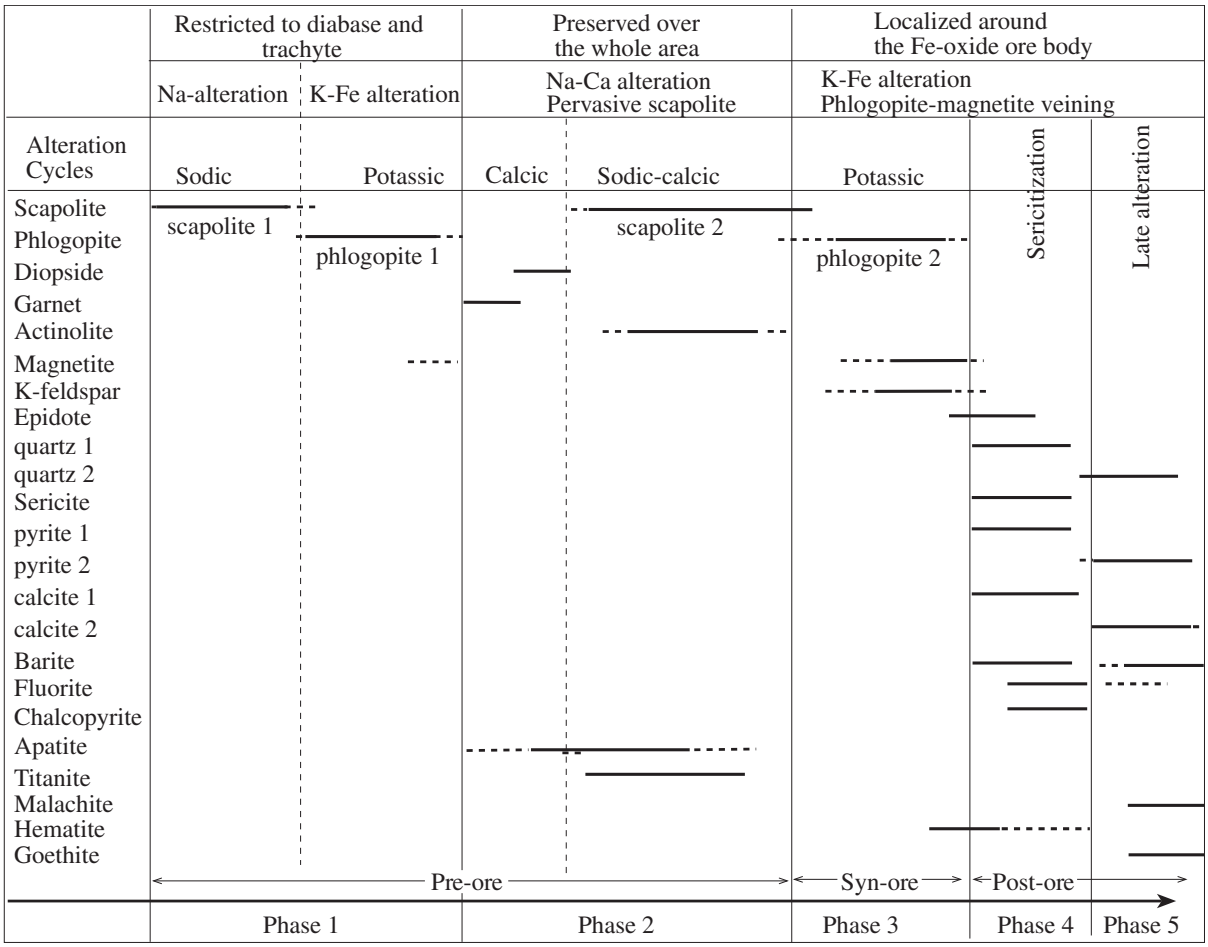

FIG. 4. Paragenetic sequence and spatial association of Na-Ca, K-Fe, sericitization, and late alteration in the Hasançelebi district. The sequence is divided into three substages: preore which refers to early Na alteration, and early K-Fe alteration and overprinting late Na-Ca alteration; synore which refers to late K-Fe alteration; postore which refers to sericitization and late alteration assemblages (solid lines refer to time at which the mineral is predominant).

TABLE 3. Summary of the Mineralogical Characteristics, Style, and Chemistry of the Main Hydrothermal Associations in the Hasançelebi District

Hydrothermal alteration	Rock types, host lithology	Mineralogy (vein and alteration)	General alteration characterictics	Hydrothermal styles	Spatial relation to Fe oxide and sulfide minerals	Comments
			Phase 1			
Premagnetite ore sodic alteration						
Na alteration scapolite 1	Diabase, trachyte	Scapolite ± actinolite	Fine-grained scapolite mainly present in altered diabase ± trachyte	Fracture controlled, fine-grained, disseminations		Restricted mainly to dike margins
Premagnetite ore potasssic alteration						
K-Fe alteration phlogopite 1	Diabase, trachyte	Phlogopite ± K-feldspar	Fine-grained phlogopite replacing scapolite	Vein-like associations	Associated with occasional magnetite dissemination	
			Phase 2			
Late sodic-calcic alteration						
Na-Ca alteration scapolite 2	Syenite, diabase, trachyte	Scapolite, diopside, garnet, actinolite, apatite, titanite	Coarse-grained, radiating crystals of scapolite, and actinolite-grained diopside and garnet	Massive to pervasive, regional alteration, structure controlled	No association with Fe oxide and sulfide mineralization	Commonly predominant at syenitic and trachytic rocks
			Phase 3			
Synmagnetite ore potassic alteration						
K-Fe alteration phlogopite 2, K-feldspar magnetite	Syenitic rocks, diabase, trachyte	Phlogopite, biotite, K-feldspar,	Medium to coarse grained phlogopite and biotite replacing scapolite	Vein-like to massive, strongly fracture controlled	Host to magnetite mineralization	Tends to increase towards microsyenite porphyry
			Phase 4			
Postmagnetite ore alteration (sericitization)						
Sericite calcite 1 Barite quartz 1 Fluorite	Trachyte, syenitic rocks	Sericite, epidote, chlorite, calcite, barite, fluorite, quartz, pyrite, hematite	Fine grained alteration of sericite, quartz and calcite replacing the main magnetite orebody	Vein breccia, localized crackle vein	Host to sulfide and hematite mineralization	Commonly associated with silicified breccia and dissemimated chalcopyrite
			Phase 5			
Late alteration						
Calcite 2 quartz 2	Trachyte, syenitic rocks	Calcite, barite, fluorite, quartz, goethite, malachite, azurite	Occurs as veins through the hematitized rocks	Vein-like, fracture controlled	Host to malachite, azurite, goethite mineralization	Localized commonly at the mine site

Stendal et al. (1995) also favor a multiphase alteration model, and they suggested that at least four generations of hydrothermal alteration took place in the district.

Phase 1 predates the magnetite ore stage and is characterized by local Na and K alteration that appears to be restricted to the immediate igneous contacts between trachyte and diabase and occasionally to trachytic rocks (Fig. 5A, B, Table 3). This phase resulted in extensive fine-grained scapolite (scapolite 1) and preore hydrothermal biotite (phlogopite 1) with or without disseminated fine-grained magnetite. In general, the mineral assemblage in phase 1 is fine grained (Fig. 6B), greenish to gray in color, overprinted almost completely by the later phases, and preserved as relict minerals replaced or enclosed by the assemblage of the phase 2 (Table 3, Fig. 4). Phase 2 is also a premagnetite stage with Na-Ca alteration (Table 3) and exhibits close time-space relationships with the syenitic intrusions (syenite, syenite porphyry and microsyenite porphyry, Fig. 5B) that cut the Hekimhan formation and Hasançelebi volcanic rocks. The assemblage in phase 2 is coarser grained, more pervasive and regional in extent. This phase consists of scapolite 2, pyroxene (diopside), garnet, and actinolite (Fig. 5F) as the predominant mineral assemblage with titanite and apatite (Fig. 6A, D, E) as accessory minerals associated with scapolite 2 (Table 3). The diabase dikes with scapolite 1 are cut by syenite porphyries containing coarser grained scapolite 2 (Fig. 5B). The assemblage consisting of

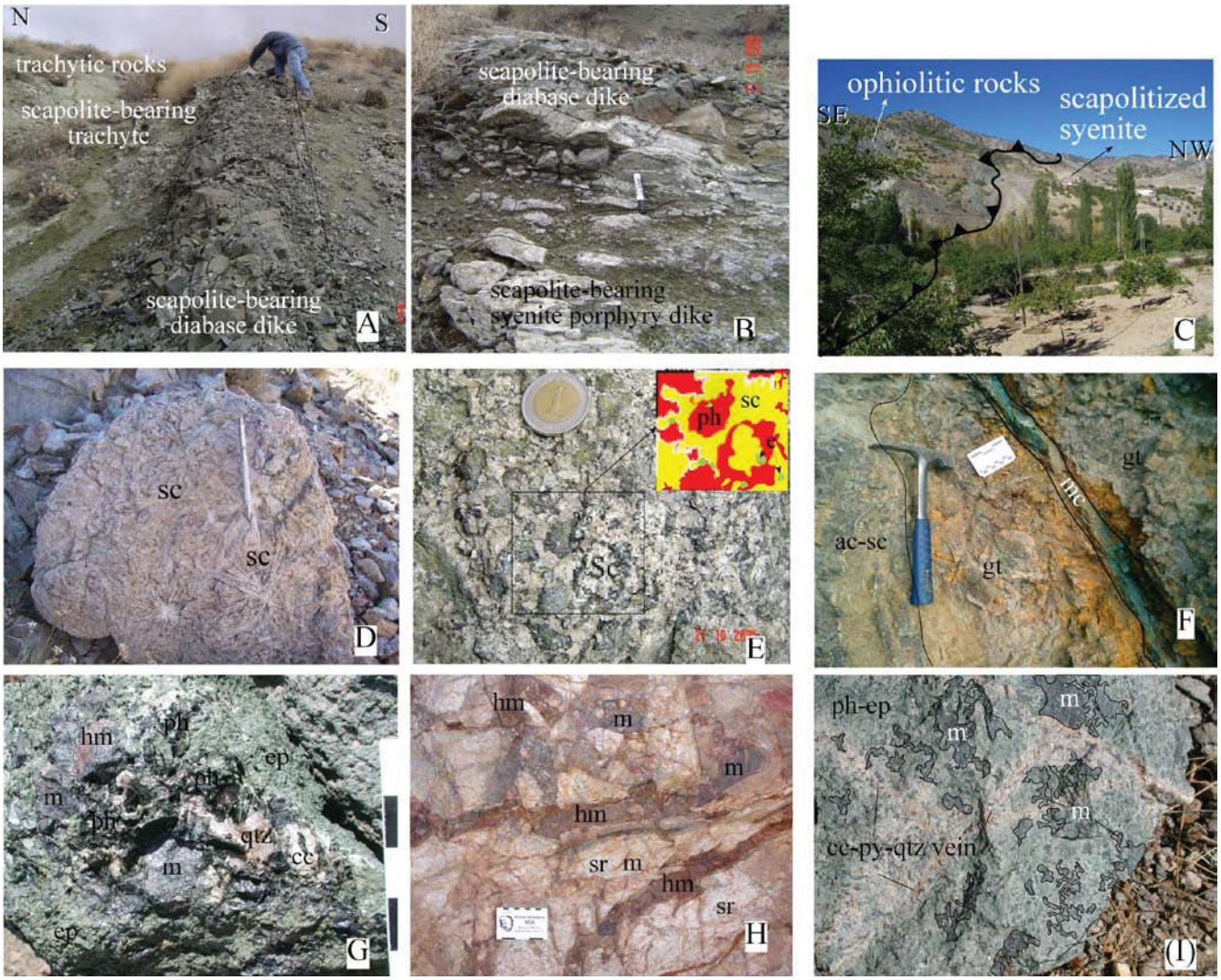

FIG. 5. Characteristic features of hydrothermal alteration and magnetite ore from the Hasançelebi district. A. East-west–trending diabase dike intruding trachytic rocks (diabase itself scapolitized). B. Scapolite-bearing diabase cut by scapolite-bearing syenite porphyry dike. C. Contact between ophiolite and scapolitized syenite. D. Syenite affected by pervasive preore Na-Ca alteration at phase 2, characterized mainly by radiating crystals of pinkish scapolite. E. Synore phlogopite (late phlogopite) replacing the scapolite within syenitic rocks, and relict scapolite (see inset for paragenetic association of scapolite and phlogopite). F. Actinolite-scapolite–altered trachytic rocks with late malachite-goethite precipitation. G. Coarse-grained phlogopite 2 with magnetite (synore K-Fe alteration), cut by calcite 1 and quartz 1 replacing scapolite 2. H. Hematite veins after magnetite within a sericitized, brecciated volcanic rock. I. Pyrite-calcite-ankerite-pyrite-quartz veining in magnetite-late phlogopite ore (ac = actinolite, cc = calcite, e = epidote, gt = goethite, m = magnetite, mc = malachite, ph = phlogopite, qtz = quartz, sc = scapolite, sr = sericite,).

scapolite 2-garnet-diopside, titanite and apatite predominates in syenitic rocks (Fig. 5D, E, H, and Table 3), whereas actinolite occurs with scapolite 2 in veins cutting the trachytic rocks (Fig. 5F). The scapolite 2 is characterized by radiating and rosette-like pink to green crystals within the syenitic rocks (Fig. 5D). The alteration assemblages formed in phases 1 and 2 are juxtaposed with the ophiolitic rocks along the east-west–trending Ciritbelen-Otmangölü fault (Fig. 5C) and normal faults to the south of the Taş and Küçüktaş hills (Fig. 2).

Phase 3 is a synmagnetite ore K-Fe alteration stage hosted by syenitic and trachytic rocks. This phase consists mainly of coarse-grained phlogopite 2 (synore phlogopite), sporadic K-feldspar, and magnetite. At a regional scale, phlogopite 2, K-feldspar, and magnetite mineralization typically postdates scapolite 2 (Figs. 5E, G, 6E-H, Table 3). Petrographical and field observations show that phlogopite 2 occurs either as veins and veinlets within the scapolite 2-rich rocks or as rims around unreplaced islands of scapolite 2 (Figs. 5E; 6G). The main magnetite mineralization is associated with synore K-Fe alteration (Figs. 5E, G, I, 6G, H).

Phase 4 is a postore magnetite sericite-quartz alteration stage (sericitization ± silicification). It consists mainly of sericite-quartz 1 ± calcite 1, clay minerals, barite, and fluorite (Figs. 4, 5H) either as veins or as replacements within the brecciated trachyte. It postdates the magnetite mineralization and marks the onset of hydrothermal brecciation as evidenced

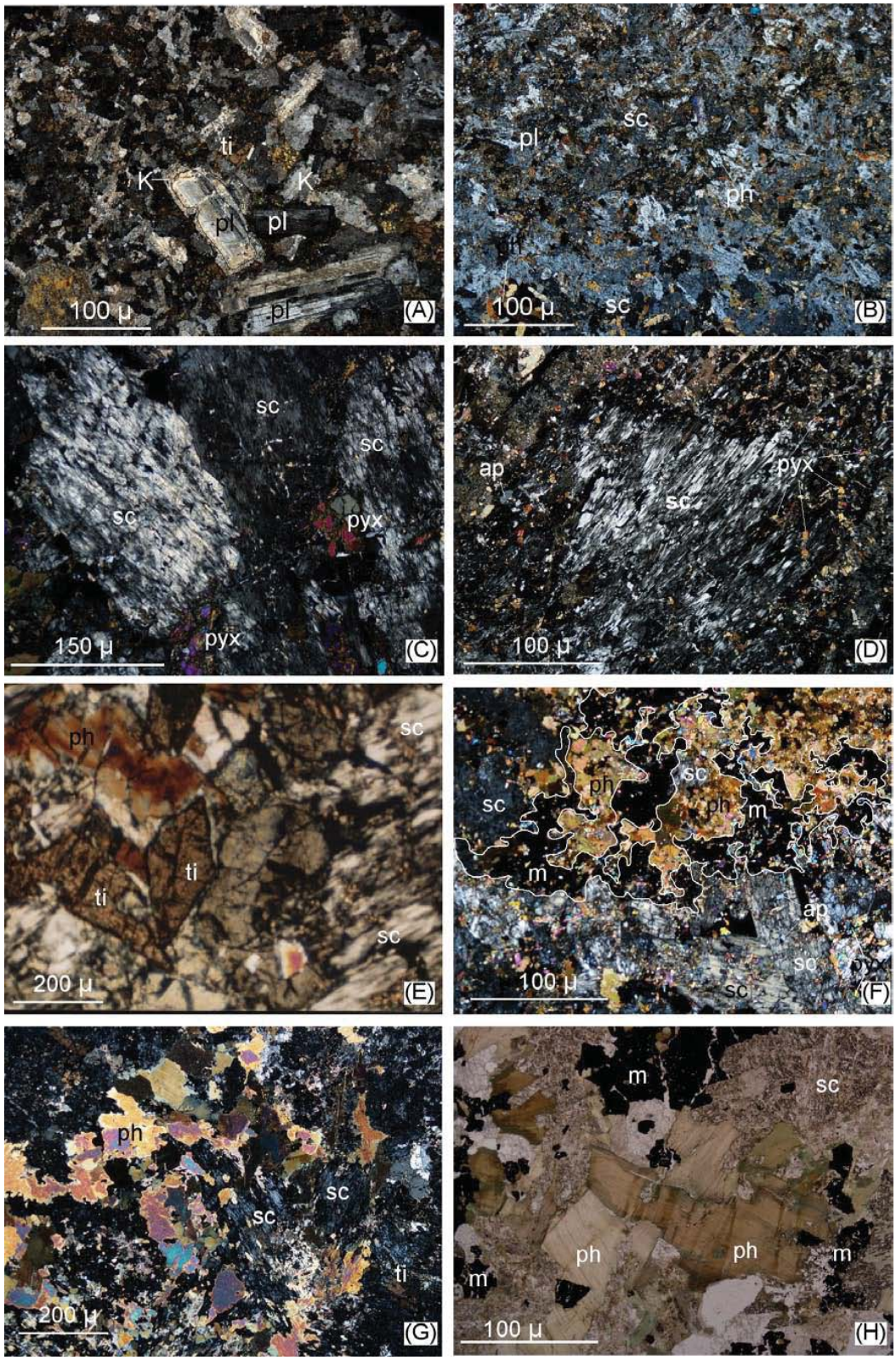

FIG. 6. Photomicrographs showing representative textures in the Hasançelebi district. A. Syenite porphyry. B. Scapolite 1 (preore Na alteration) and phlogopite 1 (preore K-Fe alteration)-bearing diabase. C. Coarse, radiating scapolite 2 replacing diopside (preore Na-Ca alteration). D. Relict diopside within scapolitized rock. E. Titanite associated with scapolite 2 and synore phlogopite (phlogopite 2). F. Fine-grained phlogopite 2 and magnetite replacing scapolite 2. G. Phlogopite 2 replacing scapolite 2. H. Coarse-grained phlogopite 2 with magnetite (synore K-Fe alteration) (ap = apatite, hm = hematite, K = K-feldspar, m = magnetite, ph = phlogopite, pl = plagioclase, pyx = pyroxene-diopside, sc = scapolite, sr = sericite, ti = titanite).

by silicified breccias within the trachytic rocks at the northern parts of the alteration immediately north of Davulgu around Küçüktaş and Taş hills (Fig. 2). It envelops the magnetite orebody and is associated with fine-grained hematite. Rare mushketovite is also reported within the silicified rocks at the open pit at the Karakuzdağ deposit (Marschik et al., 2008). Sericite, the predominant constituent of this phase, replaces the late scapolite (Fig. 5H) and occurs within the quartz veins or silicified trachytic rocks as patches or disseminations. Quartz in this phase occurs within the quartz-sericite-hematite, quartz-pyrite ± chalcopyrite or quartz-barite-calcite 1 veins cutting through synore assemblages and magnetite mineralization. The quartz-sericite-hematite, quartz 1-pyrite ± chalcopyrite veining is scarce and only related to chalcopyrite mineralization in the district. Fluorite and barite occur as sporadic minerals within the quartz-barite 1- calcite veins with or without calcite at the old underground workings to the eastern banks of Ulu stream and at the north of the open pit at the Karakuzdağ deposit.

Phase 5 is the last alteration stage and consists of veins and veinlets of calcite 2, pyrite 2, ankerite, and quartz 2, and still later supergene goethite-malachite (Fig. 5I) through the fractures within magnetite-hematite bodies and sericitized rocks.

Geochronology

Age of alteration and magmatism: U-Pb and ^{40}Ar-^{39}Ar dating

U-Pb and ^{40}Ar-^{39}Ar geochronology (Table 4, App. 1) was carried out for the main diabasic, trachytic and syenitic rocks, pre and synmagnetite ore K-Fe alteration, and ore-stage assemblages of the Hasançelebi district. Apart from Ar-Ar geochronology for volcanics by Leo et al. (1973) and Ar-Ar geochronology for hydrothermal biotite by Marschik et al. (2008), these represent a comprehensive set of geochronological data for both alteration and magmatic rocks and constrain the relative timing of alteration and magmatism in the district (Fig. 7A-H). The K-Fe alteration was dated by the ^{40}Ar-^{39}Ar method, and magmatic rocks were dated by the ^{40}Ar-^{39}Ar and U-Pb methods (Table 4).

The ^{40}Ar-^{39}Ar biotite geochronology for trachyte and trachyandesite presumed to be the oldest alkaline rocks in the district gave an age of 76.8 ± 0.7 Ma. The diabase dikes emplaced into the trachytic rocks yielded an ^{40}Ar-^{39}Ar hornblende and biotite ages of 74.4 ± 0.5 and 74.2 ± 0.6 Ma (Fig. 7; Table 4). The ^{40}Ar-^{39}Ar K-feldspar age of the syenite feldspar porphyry is 71.8 ± 0.5, within the error limits it might defines the cooling age of the syenite intrusion. The U-Pb zircon age of the microsyenite porphyry is 71.3 ± 0.3 Ma. Based on the geochronological data, it is evident that alkaline magmatism in the Hasançelebi district took place between 76.8 and 71.3 Ma.

The age for preore K-Fe alteration at phase 1 is obtained from an altered diabase, and the ^{40}Ar-^{39}Ar hydrothermal biotite (phlogopite 1) dating yielded an age of 74.3 ± 0.4 Ma, which remains within the age range for diabase intrusion (Figs. 7, 8). Two samples with and without magnetite mineralization from phase 2 and 3 from synore late phlogopite and K-feldspar altered rocks gave ^{40}Ar-^{39}Ar ages of 70.5 ± 0.42 and 68.6 ± 0.4 Ma, respectively. This suggests that alteration phases 2 and 3 took place after the syenitic and microsyenitic intrusions in the district.

Radiogenic Isotope Geochemistry

Nd and Sr isotope analysis of the host magmatic rocks and synore (phase 3) potassic alteration zones in the Hasançelebi district has been carried out. A total of six samples from host igneous rocks and synore potassic alteration were analyzed and results are given in Table 5. The altered samples are mostly from the synore K-Fe alteration with or without magnetite. They do not contain the assemblage of garnet, apatite, and titanite that retains most of the REE elements in their intracrystalline structures, as these were replaced or overprinted by synore assemblages.

Loss on ignition (LOI) ranges between 2.29 and 5.87 percent. The initial Sr and Nd isotope ratios and the initial $\varepsilon_{Sr(i)}$ and $\varepsilon_{Nd(i)}$ values were calculated based on the geochronological data in Table 4. Also given in Table 5 are the ε_{Sr} and ε_{Nd} values for each sample at the time of the formation of synore K-Fe alteration zones ($\varepsilon_{Sr(68.6)}$ and $\varepsilon_{Nd(68.6)}$).

Given the high LOI values of the host igneous rocks, the validity of any interpretation regarding the isotope compositions may, at a first glance, be questioned as most of the host rocks appear to be already altered. However, although modification can be expected in the Sr isotope systematics, Nd

TABLE 4. Ar-Ar and U-Pb Age Dating in the Hasançelebi District (the uncertainties are 2σ, except for sample 318)

		^{40}Ar-^{39}Ar			U-Pb
	Sample description	Hornblende	Biotite	K-feldspar	Zircon
Sample no.	Magmatic rocks				
318	Microsyenite porphyry	-	-	-	71.27 ± 0.29
321	Syenite feldspar porphyry	-	-	71.85 ± 0.48	-
323	Diabase dike	74.40 ± 0.51	74.26 ± 0.45	-	-
331	Trachyte, trachy-andesite	-	76.84 ± 0.67	-	-
336	Trachyte (Leylekdağ volcanics)	-	-	34.4 ± 1.1	-
	Preore K-Fe alteration (phase 1)				
328	Phlogopite rock replacing scapolite rock	-	74.32 ± 0.42	-	-
	Synore K-Fe alteration (phase 3)				
318a	Syenite porphyry veined by phlogopite	-	-	70.48 ± 0.42	-
327	Scapolite rock replaced by phlogopite-magnetite	-	-	68.64 ± 0.42	-

Note: - = not analyzed

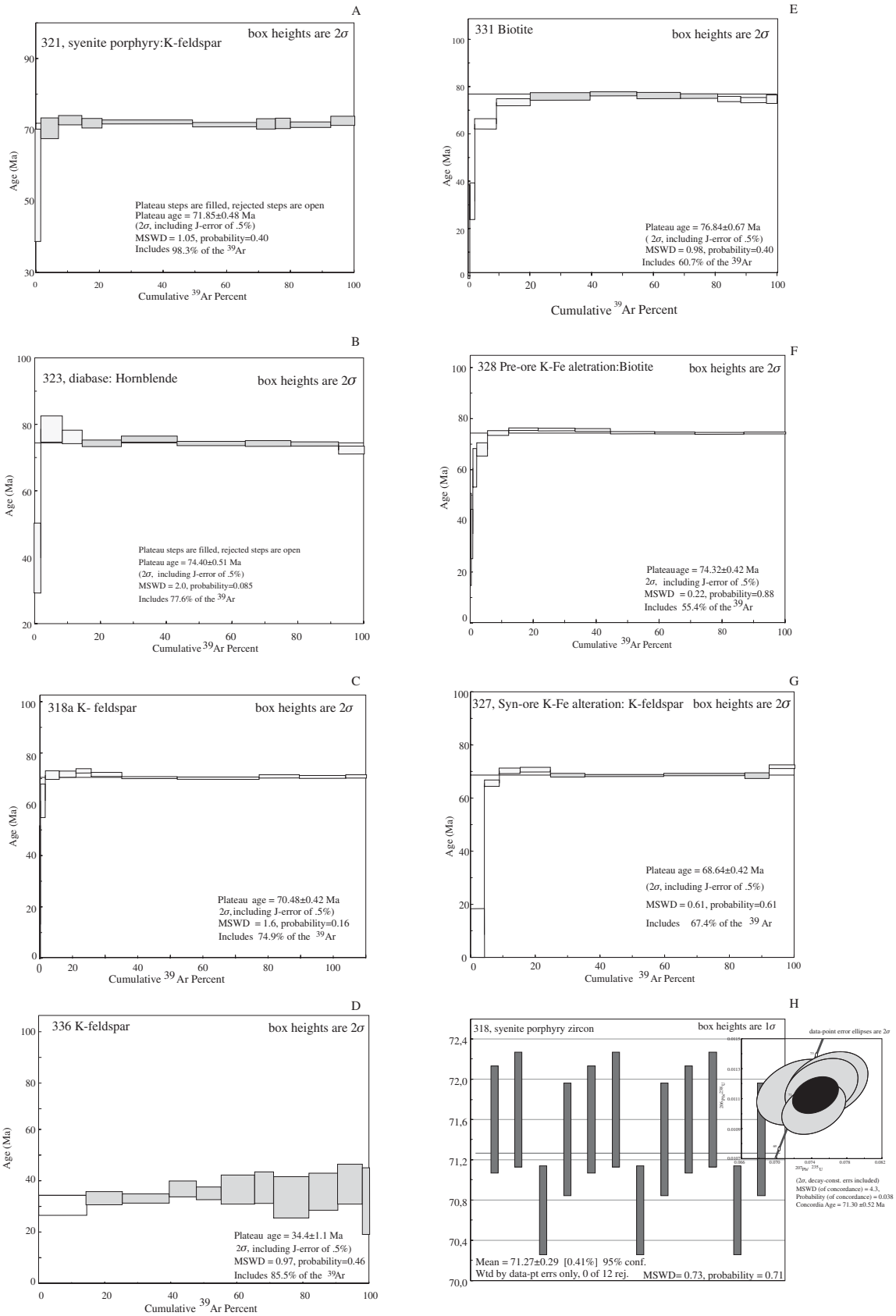

FIG. 7. $^{40}Ar/^{39}Ar$ biotite, hornblende, K-feldspar, and biotite (A, B, C, D, E, F, G) and U-Pb (H) spectra of zircon from fresh magmatic rocks and alteration.

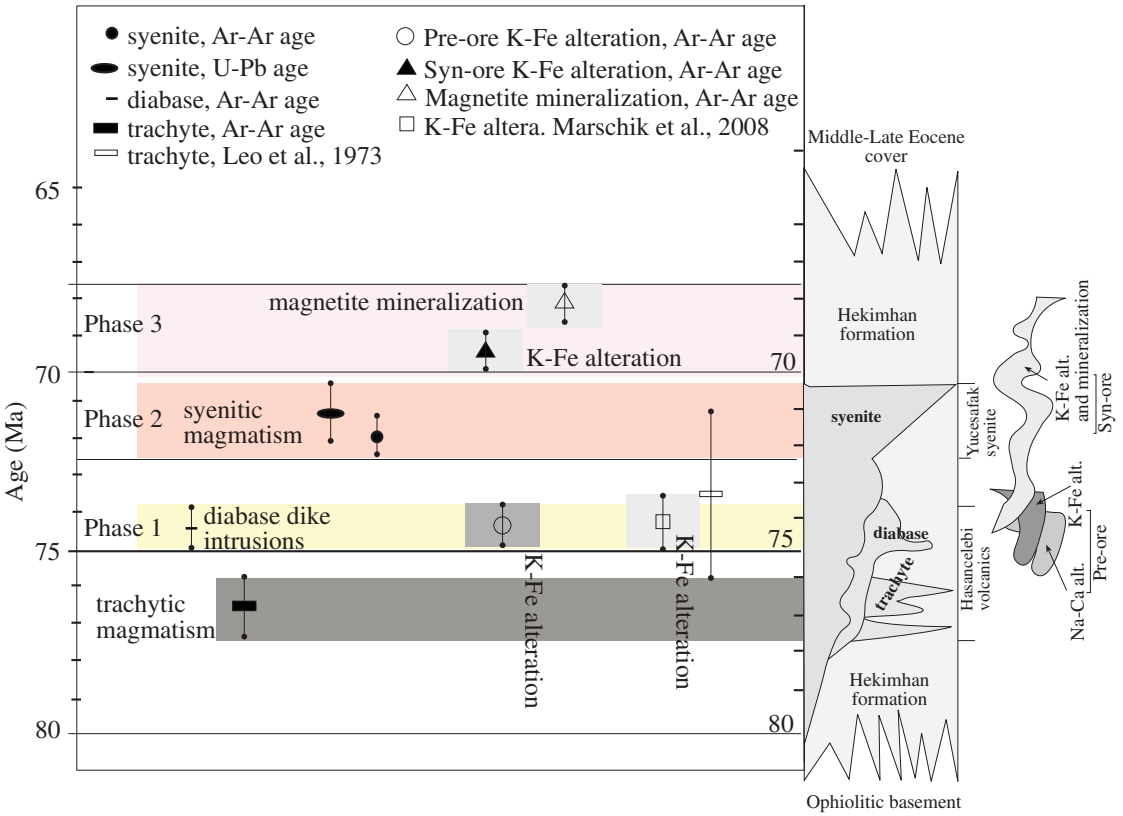

FIG. 8. Synthesis of relevant geochronological data for the Hasançelebi district (the age intervals are within the error limits).

isotope ratios are supposed to stay rather intact due to the considerably large fluid/rock ratio (>1) required to cause substantial changes in Nd isotope compositions during any hydrothermal alteration. For instance, using simple binary mixing calculations (Faure, 1986), and assigning to the possible end members $^{143}Nd/^{144}Nd$ ratios and Nd concentrations of 0.512548 and 23.3 ppm (sample 535323 in this study) and 0.512382 and $3.3*10^{-6}$ ppm (Eastern Mediterranean sea water composition; Spivack and Wasserburg, 1980; Scrivner et al., 2004), respectively, a fluid/rock = 1 results in a mixture with $^{143}Nd/^{144}Nd = 0.51254863$, which is essentially the same as the original composition [$^{143}Nd/^{144}Nd = 0.512548 \pm 5$ (2σ)] of the rock sample. In this respect, at least Nd isotope compositions can be considered as fairly reliable in a discussion of the origin of host igneous rocks.

The measured and initial isotope compositions given in Table 5 are shown in Figure 9A and B, respectively, in terms of their relative positions in isotope correlation diagrams. Also shown in the diagrams are the positions of various source regions representing different tectonic environments. As can be seen from Figure 9A and B, all the samples analyzed in this study (samples from igneous rocks and alteration zones) plot in the enriched quadrant of the isotope correlation diagram, pointing to either a metasomatized mantle source or crustal contamination in the genesis of igneous rocks and the hydrothermal fluids responsible for alteration and mineralization. For a further assessment of the possible mantle-crust interaction, variations in Nd isotope compositions are plotted against the elemental Sm/Nd ratios in Figure 9C. The rather horizontal trend in this plot is not consistent with crustal contamination during ascent of magma to surface (as this would produce a positive trend in a $^{143}Nd/^{144}Nd$ vs. Sm/Nd plot). Although the possibility of crustal contamination cannot be entirely ruled out, the fairly high initial isotope compositions (Fig. 9B) suggest that the magmatic rocks (hosting the alteration and mineralization in the Hasançelebi district) were essentially derived from a metasomatized mantle source and evolved in composition through the process of fractional crystallization (Fig. 9C) following the derivation of their parental magma from the mantle. The observation that the Nd isotope values are comparable to that of bulk Earth, while Sr values are higher and more variable (Fig. 9A) further suggests a subduction process as the responsible agent of the metasomatism in the mantle source. In fact, a subduction-modified mantle source has been proposed by several researchers for the granitoids of the Central Anatolian Crystalline Complex (İlbeyli et al., 2004; Köksal et al., 2004). Given the fact that the wall rocks and the alteration zones in the study area have overlapping $^{143}Nd/^{144}Nd$ ratios, and that substantial modification of the Nd isotope compositions by a secondary alteration process is rather difficult to achieve (requiring a fluid volume at least almost the same as that of the magmatic rocks), the hydrothermal fluids responsible for Hasançelebi mineralizations are likely to be dominated by magmatic, rather than by evaporitic fluids.

In a further attempt to constrain the source of hydrothermal fluids, we have calculated $\varepsilon_{Nd(68.6Ma)}$ and $\varepsilon_{Sr\,(68.6Ma)}$ in Table 5 to track the changes in the isotopic compositions of the magmatic rocks at the time of K-Fe alteration. Although $\varepsilon_{Sr\,(68.6Ma)}$

Table 5. Sr and Nd Isotope Data for the Hasançelebi Samples (m = measured, i = initial)

Sample	Rock type/ alteration	Age (Ma)	Sr (ppm)	Nd (ppm)	$^{87}Sr/^{86}Sr(m)$	Error (2σ)	$^{87}Sr/^{86}Sr(i)$[1]	$^{143}Nd/^{144}Nd(m)$	Error (2σ)	$^{143}Nd/^{144}Nd(i)$[1]	ε_{Sr}	ε_{Nd}	$\varepsilon_{Sr\ (68.64\ Ma)}$[2]	$\varepsilon_{Nd\ (68.64\ Ma)}$[2]
							Igneous rocks							
321	Syenite porphyry	71.85	273	49	0.710870	0.000008	0.710340	0.512497	0.000006	0.512450	79.87	–1.86	80.15	–1.90
323	Diabase	74.40	573	23.3	0.710473	0.000006	0.710123	0.512548	0.000005	0.512493	76.84	–0.94	77.13	–1.00
326	Microsyenite porphyry	71.30	175	45	0.710773	0.000006	0.710706	0.512549	0.000005	0.512492	85.06	–1.04	85.06	–1.07
331	Trachyte	76.84	439	29.2	0.710703	0.000007	0.709644	0.512563	0.000006	0.512513	70.09	–0.50	71.55	–0.60
							K-Fe alteration and mineralization							
327	K-Fe alteration	68.64	283	5.1	0.710708	0.000007	0.710634	0.512495	0.000006	0.512442	84.00	–2.08	84.00	–2.08
*329[c]	K-Fe alteration, oxide mineralization	68.64	240	14.4	0.712378	0.000007	0.709246	0.512489	0.000005	0.512446	64.29	–2.02	64.29	–2.02

[1] $^{87}Rb/^{86}Sr$ and $^{147}Sm/^{144}Nd$ values used in the determination of initial ratios were calculated using the Rb, Sr, Sm, Nd concentrations given in Table 1; atomic ratios and atomic masses used in the calculations are from Steiger and Jager (1977), Hamilton et al. (1983), Jacobsen and Wasserburg (1980), and Wapstra and Bos (1977)

[2] $\varepsilon_{Nd}=\{(^{143}Nd/^{144}Nd)_{(t)Sample}/(^{143}Nd/^{144}Nd)_{(t)CHUR}-1\}*10^4$, calculated using $^{143}Nd/^{144}Nd= 0.512638$ as present day CHUR value and $(^{147}Sm/^{144}Nd)_{CHUR} = 0.1966$. of Wasserburg et al., (1981); $\varepsilon_{Sr}=\{(^{87}Sr/^{86}Sr)_{(t)Sample}/(^{87}Sr/^{86}Sr)_{(t)BE}-1\}*10^4$, calculated using $^{87}Sr/^{86}Sr = 0.7048$ as present-day BE value and $(^{87}Rb/^{86}Sr)_{BE} = 0.087$ of O'Nions et al. (1977)

c = composite sample

values may not be considered as convincing evidence (due to possible modification of the Sr isotope compositions during alteration), the similar initial ε_{Nd} values of the K-Fe alteration and composite samples (Table 5) and of the syenite porphyry point to a genetic link between the syenitic magmatism and the hydrothermal fluids responsible for alteration and mineralization. Consequently, radiogenic isotope geochemistry, combined with geochronological data for host rocks and alteration, suggest that the alkaline magmatism which produced successive pulses of diabase and syenitic intrusions into the Hekimhan formation (Fig. 8) has been the major source for fluids responsible for the alteration and mineralization in the Hasançelebi district.

Stable Isotopes

Oxygen ($\delta^{18}O$) and hydrogen (δD) isotope analyses were carried out on six mineral separates from altered rocks. These include phlogopite, sericite, barite, calcite 1, fluorite, and quartz 1 representing the mineral associations formed during phases 1 and 4 of the hydrothermal alteration (Table 6). The $\delta^{18}O$ values of these minerals range from 8.53 to 15.13 per mil, while δD values range from –85.65 to –124 per mil (Table 6). Oxygen isotope fractionation factors for phlogopite-H_2O, muscovite and/or sericite-H_2O, quartz-H_2O (Clayton et al., 1972; Zheng 1993a), calcite-H_2O (Zheng 1993b), and barite-H_2O (Kusakabe and Robinson, 1977) were used to calculate the isotopic composition of coexisting water using maximum and minimum temperatures obtained from the fluid inclusion study by Sezerer-Kuru et al. (2006). Oxygen isotope fractionation factors used in the calculations are taken from Bowers and Taylor (1985) for calcite and phlogopite and from Suzuoki and Epstein (1976) for sericite and barite. Calculated $\delta^{18}O_{(H_2O)}$ values of the minerals are generally between 5.6 and 9.2 per mil with two lower values for barite and calcite 1 (3.1 and 2.1‰). Fractionation factor by Bowers and Taylor (1985) for calcite-1 and phlogopite and Suzuoki and Epstein (1976) for sericite and barite-1 were used to calculate $\delta D_{(H_2O)}$ values. The $\delta D_{(H_2O)}$ values define a narrow range between –80.5 to –89.2 per mil except for calcite 1 with the lowest value of –122.2 per mil.

The $\delta^{18}O$ and δD values of minerals from preore K-Fe alteration (phase 1) and postore sericitization (phase 4) plot in the magmatic water field (Taylor, 1997; Fig. 10), except for calcite 1 and barite. Similarly, the calculated values for coexisting fluids also plot in the magmatic water field, with only two samples plotting toward the formation water field. In general, the minerals exhibit a slight enrichment in $\delta^{18}O_{(H_2O)}$ and a pronounced depletion in $\delta D_{(H_2O)}$ values with decreasing temperature from K-Fe alteration to postore alteration types (Table 6).

Discussion

Comparison and correlation with IOCG -type systems

The Hasançelebi district was extensively explored for magnetite mineralization by geophysical surveys (airborne-ground magnetic surveys), and magnetic anomalies were tested by drilling. Recent works aiming at relogging of these drill cores from the deposit (Ay et al., 2004) and surface lithogeochemical surveys by Kuşcu et al. (2007c) have shown that

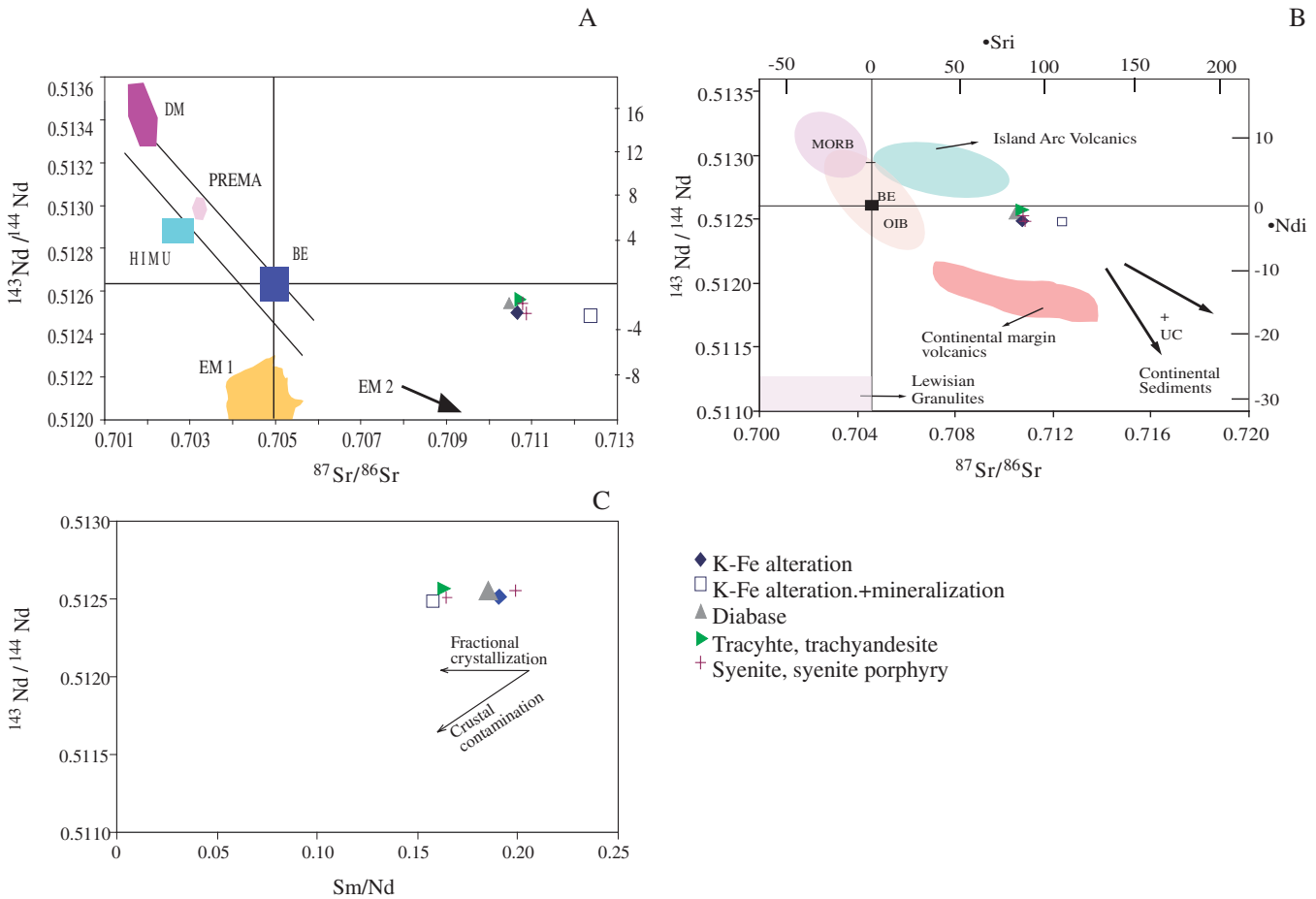

FIG. 9. Correlation diagrams for magmatic rocks and alteration. A. Nd-Sr isotope correlation. B. $^{87}Sr/^{86}Sr$ vs. $^{143}Nd/^{144}Nd$ variation. C. $^{143}Nd/^{144}Nd$ vs. Sm/Nd variation. DM = depleted mantle, EM1 = enriched mantle 1, EM 2 = enriched mantle 2, HIMU = High μ ($^{238}U/^{204}Pb$) mantle, PREMA = prevalent mantle. The tectonic and isotopic reservoir compositions are from Faure (1986) and Rollinson (1993).

the deposit contains copper (0.8–2.75%) and gold (0.04–2 g/t) and nickel (up to 1.9%), none of which have been extracted to date. Although, these are not average copper-gold grades, we believe that reassaying the core samples from suitable intervals would yield economically viable copper and gold grades. Based on comparison with the major IOCG deposits by Haynes (2000), Hitzman (2000), and Williams et al. (2005), the key features of the Fe oxide deposits in the Hasançelebi district are considered to be related to IOCG-forming hydrothermal systems The key IOCG-related features of the Hasançelebi deposit include (1) hydrothermal alteration with mineral assemblages typical of IOCG alteration, mainly along structural discontinuities, (2) although apatite is present as an accessory phase in some sodic alteration, large

TABLE 6. Hydrogen and Oxygen Isotope Analyses (‰) and Calculated Isotope Composition of Fluid

Mineral	$\delta^{18}O_{(mineral)}$(‰)	$\delta D_{(mineral)}$(‰)	T_h(°C)	$\delta^{18}O_{(H_2O)}$ (‰)	$\delta D_{(H_2O)}$ (‰)
Phlogopite 1	9.46	–89.54	700	5.61[1]	–80.54[4]
Sericite	8.87	–107.21	320–390	7.79–8.78[1]	–79.71–89.21[5]
Fluorite	8.53	–95.16	210–280	n.c	n.c
Barite	10.14	–85.65	190–380	9.25–3.13[3]	–85.65[5]
Calcite 1	12.80	–122.28	180–320	7.78–2.15[2]	–122.28[4]
Quartz 1	15.13	–124.00	290–370	6.59–7.87[2]	n.c

Notes: n.c = no calculation, Th(°C) = homogenization temperature
[1] $\delta^{18}O_{(H_2O)}$ values were calculated according to Zheng (1993a)
[2] $\delta^{18}O_{(H_2O)}$ values were calculated according to Clayton et al. (1972)
[3] $\delta^{18}O_{(H_2O)}$ values were calculated according to Kusakabe and Robinson (1977)
[4] $\delta D_{(H_2O)}$ values were calculated according to Bowers and Taylor (1985)
[5] $\delta D_{(H_2O)}$ values were calculated using experimentally determined equilibrium hydrogen isotope fractionation factors by Suzuoki and Epstein (1976)

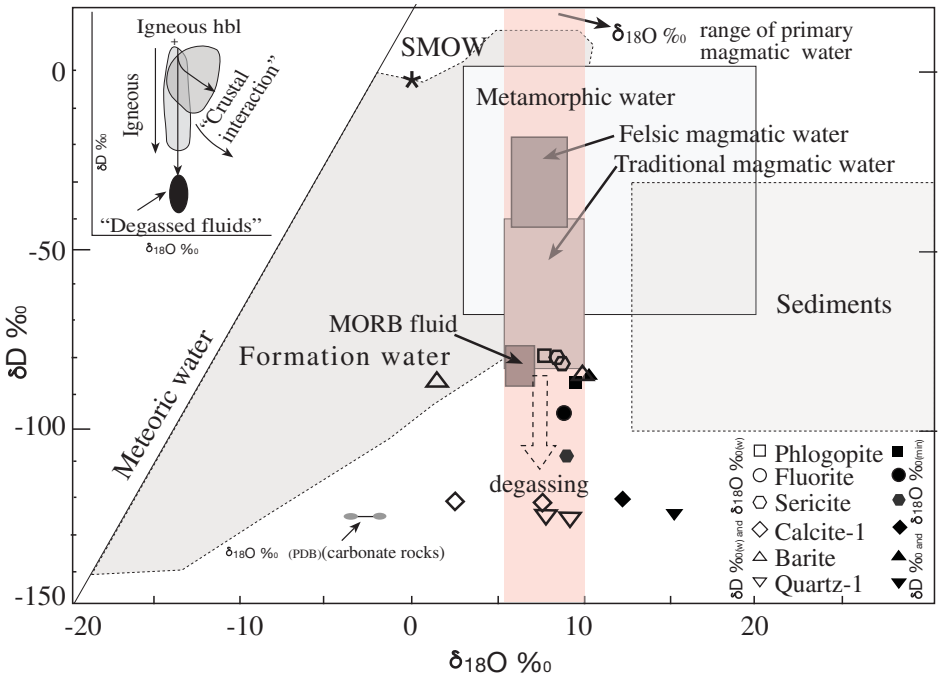

FIG. 10. Mineral and water O and H isotope compositions for alteration in the Hasançelebi district (felsic magmatic water box from Hedenquist and Lowenstern, 1994, and Taylor, 1992; metamorphic water box from Sheppard, 1986; MORB and traditional magmatic water box from Taylor, 1986; $\delta^{18}O_{(PDB)}$ values of carbonate rocks within the Hekimhan formation are from Yıldız and Özdemir (1999) (open patterns refer to $\delta^{18}O$ values for water (w) and filled patterns refer to $\delta^{18}O$ and δD values for minerals (min)).

magnetite-apatite deposits of the Kiruna type (Hitzman et al., 1992; Hitzman, 2000; Williams et al., 2005) do not appear to be present in the Hasançelebi district, (3) Fe oxide mineralization is predominant, and magnetite is commonly associated with potassic alteration, while hematite accompanies late-stage hydrolytic alteration and carbonatized rocks, (4) sulfides are predominantly Fe- and occasionally Cu-bearing in the pyrite-calcite ± chalcopyrite, quartz-pyrite, and barite-calcite veins and veinlets, and U is (Uçurum et al., 1996) elevated in some parts, (5) alteration and mineralization occur as epigenetic magnetite, magnetite-hematite, and pyrite-calcite ± chalcopyrite, and barite-calcite-pyrite veins, replacements, and disseminations hosted by pervasively altered alkaline rocks, and diabasic and syenitic intrusions of Late Cretaceous age, (6), Fe and Cu sulfide veins are hosted by ironstones, mainly by sericitized maghemitized rocks, and (7) the host rocks and alteration are confined to crustal scale regional strike-slip and normal faults or shear zone.

Relationship to other Fe oxide deposit types (Kiruna type)

Kiruna-type ore deposits are characterized by the sulfide-poor mineral assemblage of low-Ti magnetite-fluorapatite-actinolite and range in size from large bodies containing many hundreds of millions of metric tons of high-grade iron ore, to small veins and veinlets (Hildebrand, 1986). Although, Hitzman et al. (1992) classified the Kiruna-type deposits in the IOCG class, this definition was refined later by Hitzman (2000) and Williams et al. (2005), and they suggested that Kiruna-type Fe oxide deposits and Fe skarns are not IOCG deposits but share many characteristics (Williams et al., 2005), including: (1) coexistence in some metallogenic provinces where other types of ore deposits are rare, (2) common association with large-scale alkali, particularly sodic alteration systems, and (3) overlapping minor element association (e.g., Cu, Au, P, F, REE, U). IOCG deposits commonly have space-time association with the other Fe oxide-bearing deposits like Kiruna-type and Fe skarns. This association is considered to be particularly striking by similarities in alteration mineralogy and the Fe oxide-rich and Cu-poor nature of these deposits compared to the true Cu-rich IOCG type.

Kiruna-type Fe oxide-apatite ores and Fe skarns may share certain characteristics with IOCG deposits. For example, the apatite-bearing Fe oxide ores in Kiruna-type deposits of northern Sweden have a distinct association with sodic and potassic alteration (Frietsch et al., 1997; Martinsson, 1997) and anomalous concentrations of the REE (e.g., Frietsch and Perdahl, 1995). The overall paragenesis is closely comparable to the IOCG-type deposits. The Cu-Au mineralization spatially related to the Kiruna-type ores closely corresponds to Na-(Ca-Fe) alteration overprinted by high-temperature K-Fe alteration with late-stage, low-temperature K-Fe-H-CO_2 alteration, or is commonly associated with calcite and ankerite alteration. This distinction between Kiruna-type ores and the Hasançelebi district is largely based on the following:

1. The common occurrence of enrichment of U-Th, heavy rare earth elements, and F-Ba assemblages hosted by hydrolytic alterations in the Hasançelebi district (Kuluncak area to the northwest of the Karakuz magnetite-hematite deposit (Uçurum et al., 1996; Ay et al., 2004).

2. The lack of abundant apatite, a distinctive constituent in the Kiruna-type ores. Apatite in the Hasançelebi district occurs only as minute inclusions associated with scapolite within the Na-Ca alterations and has no spatial association with the Fe oxide mineralization in contrast to Kiruna-type deposits. Unlike the Kiruna-type Fe oxide deposits, the magnetite and hematite mineralization in the Hasançelebi district clearly postdates the apatite-bearing sodic-calcic assemblage and has a spatial and temporal association with the potassic and hydrolytic alterations, respectively.

3. Alteration in the Hasançelebi district occupies about 70 km² compared to spatially restricted alterations in Fe skarns.

4. Likewise, the common occurrence of chalcopyrite associated with the late stages of potassic alteration in Kiruna-type ores (Williams et al., 2005) is critical in discriminating the Fe oxide deposits in the Hasançelebi district from Kiruna-type deposits; since the sulfides are not temporarily and spatially associated with the potassic alteration in the Hasançelebi district.

Unlike the Kiruna-type deposits, the stable and radiogenic isotope analyses suplemented by Ar-Ar and U-Pb geochronology provide evidence for synchronous magmatic activity (alkaline in nature) in the Hasançelebi district. Furthermore, Uçurum et al. (1996) did not favor a Kiruna-type mineralization style in the Hasançelebi and Karakuz Fe oxide deposits primarily based on the lower total alkali content (9–13 wt%) of mineralized trachyte-trachy-andesites with Na_2O less than 1 percent of the total alkalies and P_2O_5 concentration less than 0.5 percent in all of the host-rock samples compared to Kiruna-type deposits. They also suggested that low sodium and phosphorus contents of the Karakuz iron deposit indicate a different origin of the Karakuz deposit compared to Kirunavaara in Sweden or Kiruna-type deposits elsewhere in the world.

Petrogenesis of alkaline magmatism and tectonic setting

The geochemical characteristics and trace element ratios of the Hasançelebi volcanic rocks and the Yüceşafak syenite are consistent with within-plate magmatism derived from a metasomatized mantle source (Fig. 2E, F). Th/Yb vs. Ta/Yb (Fig. 2G) indicates that magmas derived from a mantle source which was either previously enriched by small-degree partial melts (displacement along the mantle array) and/or was metasomatized during ancient subduction. Likewise, the displacement of all samples toward higher Th/Yb ratios in Figure 2G supports enrichment during an older subduction event. Earlier works (Yılmaz et al., 1993; Kuşcu et al., 2007b-d; İlbeyli and Özgenç, 2008) also confirmed that the parental magmas are alkaline in nature and were generated from mantle sources, modified by a subduction component within the Hasançelebi district. İlbeyli and Özgenç (2008) noted that the syenitic rocks have Zr/Hf and Nb/Ta ratios indicating an enriched mantle source. The enrichment during earlier subduction or effect of crustal contamination can be best observed on combined Yb/Ta vs. Y/Nb (Whalen et al., 1987; Best and Christiansen, 2001) and Nb/Th vs. Nb plots (Fig. 2H, I). The linear trends observed in Figure 2G, H, and J are suggestive of crustal contamination of a mantle-derived basaltic melt. The melt source is likely to be lithospheric mantle based on La/Nb ratios greater than 1.0 (De Paolo and Daley, 2000; Fig. 2J). These magmas resulted from partial melting within an extension-dominated regime (Kuşcu et al., 2007b, d) following the major collision between the Eurasian and Afro-Arabian plates. This is also evidenced by the basin development and associated coeval magmatism within the Hekimhan basin.

Spatial and temporal association between alteration and alkaline magmatism

In the Hasançelebi district, pervasive preore Na-Ca and pre- to synore K-Fe alteration was overprinted by postore sericite-quartz and late alteration in multiple, overprinting systems at 700° to 130°C. The period of hydrothermal alteration and mineralization (ca. 74–68 Ma) overlaps with that of alkaline magmatism (ca. 76–71 Ma) in the Hasançelebi district. The emplacement of diabase and syenite and/or microsyenite porphyry intrusions into the Hekimhan basin was the driver of regional hydrothermal systems and played an important part in the formation of the Hasançelebi Fe oxide-(Cu-Au) mineralization. The emplacement of diabase dikes into the trachytic rocks and coeval sedimentary sequences resulted in the early generation (phase 1) of sodic and potassic alteration restricted mainly to marginal parts of the trachytic rocks and diabases. The emplacement of syenite porphyry, and microsyenite porphyry dikes into sedimentary sequences, syenitic and trachytic, diabasic rocks, resulted in pervasive and regional preore Na-Ca and and synore K-Fe alteration (phases 2 and 3) of these rocks.

The U-Pb and ^{40}Ar-^{39}Ar geochronology of the igneous rocks and potassic alteration in phases 1 and 2 contribute much to our understanding of the temporal associations between alteration and alkaline magmatism within the Hasançelebi district and the source of fluids. The results of U-Pb zircon and Ar-Ar biotite-hornblende geochronology show that alteration assemblage of phase 1 formed during a period ranging from ca. 74.4 to 74.3 Ma, was overprinted by alteration formed during phases 2, 3, and 4, which took place between 71.3 and 68.6 Ma. The 74.4 Ma ^{40}Ar-^{39}Ar hornblende age for diabase intrusion and the 74.3 Ma ^{40}Ar-^{39}Ar biotite age for phlogopite 1 clearly shows that the preore potassic (K-Fe) alteration during phase 1 exhibit an overlap with the age of diabase dikes and hence inferred to be temporally related to emplacement of these dikes. The ^{40}Ar-^{39}Ar K-feldspar geochronology of the phlogopite- and phlogopite-magnetite–bearing syenitic rocks show that the age of synore K-Fe alteration in the district is between 70.5 ± 0.4 and 68.6 ± 0.4 Ma. These ages overlap with the age (including uncertainties) of syenitic magmatism in the district (Fig. 8). Consequently, Ar-Ar and U-Pb geochronology on syenitic rocks and synore K-Fe alteration zones favors an evolution where the synore K-Fe alteration (phase 3) is temporally related to the emplacement of syenitic dikes, or to fluids derived directly from the crystallizing syenitic magma. Trachyte and trachy-andesite (76.8 ± 0.67 Ma) are older than other igneous rocks, and the alteration assemblages formed during each phase. Consequently, a temporal and genetic link between the alteration and trachytic magmatism is unlikely.

Timing of mineralization

The paragenetic association of alteration and mineralization indicates that iron oxide and Cu ± Au mineralization postdate the preore Na-Ca alteration that formed at ca. 74.3

Ma. In an earlier study by Marschik et al. (2008), the Ar-Ar biotite ages of 73.4 ± 0.4 and 74.9 ± 0.4 Ma (2σ) from K-Fe alteration associated with magnetite mineralization are interpreted as the mineralization age. If their interpretation is correct, then there should be an earlier magnetite mineralization related to phase 1 defined in this work. We have no data to support an earlier generation of magnetite mineralization, and this needs futher investigation in the district. One possibility is the occurrence of rare magnetite disseminations associated with the phlogopite 1 formed during preore K-Fe alteration. Yet, hydrothermal biotite from a vein cutting the scapolitized host rocks yielded an Ar-Ar mean plateau age of 73.1 ± 0.8 Ma (2σ; Marschik et al., 2008) and is comparable to our Ar-Ar biotite ages related to K-Fe alteration during phase 1. Therefore, it may correspond to the preore K-Fe alteration formed during phase 1. Our ^{40}Ar-^{39}Ar K-feldspar geochronology of the phlogopite- and phlogopite-magnetite–bearing syenitic rocks yielded an age range between 70.5 ± 0.4 and 68.6 ± 0.4 Ma, suggesting that the age of synore K-Fe alteration and mineralization formed during this interval.

Implications for fluid source: REE, radiogenic and stable isotope constraints

The REE compositions and patterns, the isotopic signatures of hydrothermal alteration, and the associated igneous rocks help constrain interpretations of the source and possible role of the fluids in the Hasançelebi district.

As has been shown in the geochemistry section, the least altered syenite porphyry rocks and the samples from synore K-Fe alteration displays similar or almost the same chondrite-normalized REE patterns (despite the relatively lower enrichment level in the latter; Fig. 2C), and this suggests that the igneous host rocks did not undergo exchange reactions with fluids other than coeval magmatic fluids during K-Fe alteration. It is highly likely that any fluid other than the coeval magmatic fluids would have modified the REE composition of igneous rocks, which is not the case in this work.

The stable and radiogenic isotopes have been useful as hydrothermal fluid tracers, although they are to some degree open to water-rock reactions along the pathways. Studies utilizing radiogenic isotopes (Pb, Nd, Sr) on mineralized systems are numerous as reviewed by Johnson and McCulloch (1995), Campbell et al. (1998), and Gleason et al. (2000). It is highly likely that the alteration zones and their magmatic hosts should have similar isotope systematics if the fluids involved in the alteration and mineralization are released from a crystallizing and cooling magma. The Nd-Sr isotope system is therefore critical to unravel fluid characteristics and sources. Deposits formed in association with the introduction of magmatic fluids should exhibit overlaps in their isotopic composition, as is the case in the Hasançelebi district. The initial ε_{Ndi} values of the K-Fe alteration and a composite sample (samples 327 and 329, respectively) range from –2.02 to –2.08, close to the calculated ε_{Nd} value of associated syenite porphyry at the time of alteration ($\varepsilon_{Nd\ (68.6Ma)}$–1.90; Table 5). These ε_{Nd} values are far higher than ε_{Nd} values of crustal rocks (see Skirrow et al., 2007), indicating that the external (crustal-derived) fluids have not been involved during K-Fe alteration. Instead, fluids at the time of K-Fe alteration appears to have an igneous source, preferentially from mafic rocks (i.e., diabase). Similar results have also been obtained in four igneous-related Fe oxide-hosted (Fe-P-REE) systems in North America by Gleason et al. (2000). They concluded that the common pattern of REE and identical Nd isotope compositions of altered rocks and coeval igneous host rocks indicate that the latter is the primary source of REE in all four regions and is inconsistent with a significant contribution of REE from other sources. Likewise, Johnson and McCulloch (1995) showed that Nd isotope data imply a mantle source of REE and therefore possibly for other ore components at Olympic Dam. The ε_{Nd} data from IOCG deposits from several independent studies by Skirrow (1999, 2000), Skirrow et al. (2007) and Gleason et al. (2000), are permissive of parental fluids of ultimately magmatic origin for high-temperature, magnetite-K-feldspar calc-silicate alteration. For example, ε_{Nd} values of around -2 is interpreted to reflect input of REE from mafic rocks in the West Peko deposit (Skirrow, 1999, 2000).

The stable isotope composition of the fluid calculated from the mineral-water pairs (Table 6) indicates a fluid of dominantly magmatic origin (Fig. 10). The slight enrichment in $\delta^{18}O_{(H_2O)}$ and a pronounced depletion in $\delta D_{(H_2O)}$ values (Table 6) could be ascribed to magmatic degassing, or open-system interaction with other, preferentially meteoric waters (Meinert et al., 2003; Fig. 10). Magmatic degassing occurs in the roof of shallow intrusions due to onset of hydrothermal fracturing or adiabatic decompression (Friedman and O'Neil, 1977; Taylor, 1988; Shmulovich et al., 1999). This results mostly in depletion in $\delta D_{(H_2O)}$ and little or no change in $\delta^{18}O_{(H_2O)}$ (Fig. 10). In the case of interaction between magmatic and external (crustal derived) fluids, the isotope compositions would plot along a curved trend toward more enriched $\delta^{18}O_{(H_2O)}$ and depleted $\delta D_{(H_2O)}$ isotope compositions in the $\delta^{18}O_{(H_2O)}$ - $\delta D_{(H_2O)}$ diagram (Fig. 10, inset, Mark et al., 2004a). However, our results show that the fluids associated with K-Fe alteration and postore sericitization defined an almost vertical isotopic trend (with the exception of two postore samples shifting toward the formation water field), supporting a dominantly magmatic origin for hydrothermal fluids. However, it is reasonable to assume that there might be isotopic exchange at least partly due to interaction between variably degassed magmatic fluids and the crustal rocks or external fluids, following hydrothermal fracturing and consequent degassing and/or boiling during postore sericitization. Given that the postore sericitization was followed and overprinted by late alteration (phase 5), we suggest that the alteration at phase 5 could also have been formed at least in part by interaction of degassed fluids and external fluids (crustal and/or basinal brines). This is supported by the sulfur isotope composition of pyrite ($\delta^{34}S_{(VCDT)}$ 16.0 and 17.4‰; Marschik et al., 2008) within calcite veins replacing the magnetite orebody, which imply a nonmagmatic origin of sulfur (seawater or marine evaporitic source) at least for the late alteration (phases 4–5).

Conclusions

The alteration patterns, spatial and temporal association of the alteration assemblages along with the main sodic-calcic alteration, the Fe oxide mineralization, and overprinting sericite-hematite-quartz alteration suggest that Hasançelebi iron oxide deposits share many characteristics with IOCG systems. The REE patterns, radiogenic and stable isotope systematics,

and spatial and temporal association between the igneous rocks and alteration assemblages are in favor of a genetic link between the alteration and/or mineralization and intrusion of diabase dikes and syenite porphyry-microsyenite porphyry. Our U-Pb and ^{40}Ar-^{39}Ar geochronology of the igneous rocks and potassic alteration in phases 1, 2, and 3 show that the magmatism and alteration-mineralization took place between 74.4 and 68.64 Ma. We argue that the data obtained from the present study are not consistent with models envisaging a nonmagmatic fluid origin for the alteration system in the Hasançelebi deposit as proposed by Marschik et al. (2008). Instead our data on REE composition and pattern, and isotopic signatures of hydrothermal alteration, stable isotope compositions ($\delta^{18}O$ and δD), and the associated igneous rocks provide evidence for a magmatic source of fluids responsible for the pre- and synore alteration in the Hasançelebi district, although a basinal brine or even an evaporitic source component cannot be ruled out, particularly for postore alteration. However, further research involving alternative techniques to those presented here (e.g., PIXE, Br/Cl, and Sr/Cl isotope analysis of fluid inclusions) is clearly required and may contribute further to the understanding of the genesis and sources of fluids in the Hasançelebi district.

Acknowledgments

This work received financial support from the Scientific Research Council of Turkey (TÜBİTAK, grant ÇAYDAG-103Y023), and partly from the General Directorate of Mineral Research and Exploration (MTA), and Turkish Petroleum Corporation (TPAO). We gratefully acknowledge the support of these organizations. Haroldo Lledo reviewed an earlier version of the manuscript. This paper benefited from constructive comments and suggestions by Mark Barton and Tim Baker. The manuscript was greatly improved as a result of reviews by Roger Skirrow and Bruce Eglington. The editorial handling by Jean Cline and Larry Meinert is gratefully acknowledged, and we thank them for suggesting significant improvements.

REFERENCES

Ay, Y., Yıldırım, S., Dumanlılar, O., Turgut, O., Tablacı, A., Yıldız, H., Dumanlılar, H., 2004, Olimpik Dam tipi Fe-oksit-Cu-Au-(Ag-Ba- U-Th-REE) yataklarına Türkiye'den bir örnek: Hasançelebi Fe yatağı: Geological Congress of Turkey, 57th, Ankara, p. 107–108 (in Turkish with English abs.).

Barton, M.D., and Johnson, D.A, 1996, Evaporitic source model for igneous related Fe oxide-(REE-Cu-Au-U) mineralization: Geology, v. 24, p. 259–262.

Best, M., and Christiansen, E.H., 2001, Igneous petrology: Ann Arbor, Blackwell Science, 458 p.

Beyarslan, M., and Bingol, A.F., 2000, Petrology of a supra-subduction zone ophiolite (Elazıg, Turkey): Canadian Journal of Earth Sciences, v. 37, p. 1411–1424.

Bodnar, R.J., 1993, Revised equation and table for determining the freezing point depression of H_2O-NaCl solutions: Geochimica et Cosmochimica Acta, v. 57, p. 683–684.

Bowers, T.S., and Taylor, H.P. , Jr.1985, An integrated chemical and stable isotope model of the origin of midocean ridge hot spring systems: Journal of Geophysical Research, v. 90, p. 12583–12606.

Campbell, I.H, Compston, D.M, Richards, J.P, Johnson, J.P, and Kent, A.J.R., 1998, Review of the application of isotopic studies to the genesis of CuAu mineralization at Olympic Dam and Au mineralization at Porgera, the Tennant Creek district and Yilgarn craton: Australian Journal of Earth Sciences, v. 45, p. 201–218.

Carten, R.B., 1986, Sodium-calcium metasomatism: Chemical, temporal and spatial relationships at the Yerington, Nevada, porphyry copper deposit: Economic Geology, v. 81, p. 1495–1519.

Channel, J., and Kozur, H., 1997, How many oceans? Meliata, Vardar, and Pindos oceans in Mesozoic Alpine paleogeography: Geology v. 25, p. 183–186.

Chiaradia, M., Banks, D., Cliff, R., Marschik, R., and de Haller, A., 2006, Origin of fluids in iron oxide-copper-gold deposits: Constraints from $\delta^{37}Cl$, $^{87}Sr/^{86}Sr$ and Cl/Br: Mineralium Deposita, v. 41, p. 565–573.

Clayton, R.N., O'Neil, J.R., and Mayeda, T.K., 1972, Oxygen isotope exchange between quartz and water: Journal of Geophysical Research, v. 77, p. 3057–3067.

Cox, K.G., Bell, J.D., and Pankhurst, R.J., 1979, The interpretation of igneous rocks: London, Boston, George Allen and Unwin, 450 p.

Craig, H., 1961, Isotopic variations in meteoric waters: Science, v. 133, p. 1702–1703.

De Jong, G., and Williams, P. J., 1995, Giant metasomatic system formed during exhumation of mid-crustal Proterozoic rocks in the vicinity of the Cloncurry fault, northwest Queensland: Australian Journal of Earth Sciences, v. 42, p. 281–290.

DePaolo, D.J., and Daley, E.E., 2000, Neodymium isotopes in basalts of the southwest basin and range and lithospheric thinning during continental extension: Chemical Geology, v. 169, p. 157–185.

Dilles, J.H., and Einaudi, M.T., 1992, Wall-rock alteration and hydrothermal flow paths about the Ann-Mason porphyry copper deposit, Nevada: A 6–km vertical reconstruction: Economic Geology, v. 87, p. 1963–2001.

Faure, G., 1986, Principles of isotope geology, New York, Wiley, 589 p.

Friedman, I., and O'Neil, J.R., 1977, Data of geochemistry. Compilation of stable isotope fractionation factors of geochemical interest: U.S.Geological Survey Professional Paper 440–KK, p. 1–12.

Frietsch, R., and Perdahl, J.A., 1995, Rare earth elements in apatite and magnetite in Kiruna type iron ores and some other iron ore types: Ore Geology Review, v. 9, p. 489–510.

Frietsch, R., Tuisku, P. , Martinsson, O., and Perdahl, J.A., 1997, Early Proterozoic Cu-(Au) and Fe ore deposits associated with regional Na-Cl metasomatism in northern Fennoscandia: Ore Geology Reviews, v. 12, p. 1–34.

Gleason, J.D., Marikos, M., Barton, M.D., and Johnson, D.A., 2000, Neodymium isotopic study of rare earth element sources and mobility in hydrothermal Fe oxide (Fe-P-REE) systems: Geochimica et Cosmochimica Acta, v. 64, p. 1059–1068.

Goldstein S.L., O'Nions, R.K., and Hamilton, P. J., 1984, A Sm-Nd study of atmospheric dusts and particulates from major river systems: Earth and Planetary Science Letters, v. 70, p. 221–236.

Gürer, Ö.F., 1992, Hekimhan-Hasançelebi (Malatya) Dolaymın Jeolojisi: Unpublished dissertation, İstanbul University Pure and Applied Sciences (in Turkish with English abs.), 323 p.

——1996, Geological position and the genesis of Hasançelebi alkaline magmatism at the eastern Taurides (NW Malatya): Turkish Journal of Earth Sciences, v. 5, p. 71–88.

Gürer Ö.F, and Aldanmaz, E., 2002, Origin of the Upper Cretaceous-Tertiary sedimentary basins within the Tauride-Anatolide platform in Turkey: Geological Magazine, v. 139, p. 191–197.

Hamilton, P.J., O'Nions, R.K., Bridgwater, D., and Nutman, A., 1983, Sm-Nd studies of Archaean metasediments and metavolcanics from West Greenland and their implications for the Earth's early history: Earth and Planetery Science Letters, v. 62, p. 263–272.

Haynes, D.W., 2000, Iron oxide copper gold deposits: Their position in the ore deposit spectrum and modes of origin, *in* Porter, T.M., ed., Hydrothermal iron oxide copper-gold and related deposits: A global perspective: Adelaide, Australian Mineral Foundation, p. 71–90.

Haynes, D.W., Cross, K.C., Bills, R.T., and Reed, M.H., 1995, Olympic Dam ore genesis: A fluid-mixing model: Economic Geology, v. 90, p. 281–307.

Hedenquist, J.W., and Lowenstern, J.B., 1994, The role of magmas in the formation of hydrothermal ore deposits: Nature, v. 370, p. 519–526.

Hildebrand, R.S., 1986, Kiruna-type deposits: Their origin and relationship to intermediate subvolcanic plutons in the Great Bear magmatic zone, northwest Canada: Economic Geology, v. 81, p. 640–659.

Hitzman, M.W., 2000, Iron oxide-Cu-Au deposits: What, where, when, and why, *in* Porter, T.M., ed., Hydrothermal iron oxide copper-gold and related deposits: A global perspective: Adelaide, Australian Mineral Foundation, p. 9–25.

Hitzman M.W., Oreskes, N., and Einaudi, M.T., 1992, Geological characteristics and tectonic setting of Proterozoic iron oxide (Cu-U-Au-REE) deposits: Precambrian Research, v. 58, p. 241–287.

Hunt, J.A., Baker, T., and Thorkelson, D.J., 2007, A review of iron oxide copper-gold deposits, with focus on the Wernecke breccias, Yukon, Canada, as an example of a non-magmatic end member and implications for IOCG genesis and classification: Exploration and Mining Geology, v. 16, p. 209–232.

İlbeyli, N., and Özgenç, I., 2008.Geochemical constraints on petrogenesis of Late Cretaceous alkaline magmatism in east-central Anatolia (Hasançelebi-Basören, Malatya), Turkey: Mineralogy and Petrology, DOI 10.1007/s00710-008-0027-0.

İlbeyli, N., Pearce, J., Thirlwall, A.M.F., and Mitchell, J.G., 2004, Petrogenesis of collision-related plutonics in Central Anatolia, Turkey: Lithos, v. 72, p. 163–182.

İzdar, E.K., and Ünlü, T., 1985, Hekimhan-Hasançelebi-Kuluncak bölgesinin jeolojisi: Piri Reis International Contribution Series Publication 2, p. 303–329.

Jacobsen, S.B., and Wasserburg, G.J., 1980. Sm-Nd isotopic evolution of chondrites. Earth and Planetary Science Letters, v. 50, p. 139–155.

Johnson, J.P. , and McCulloch, M.T., 1995, Sources of mineralizing fluids for the Olympic Dam deposit, (South Australia): Sm-Nd isotopic constraints: Chemical Geology, v. 121, p. 177–199.

Kaymakçı, N., Inceoz, M., and Ertapınar, P. , 2006, 3D-architecture and Neogene evolution of the Malatya basin: Inferences for the kinematics of the Malatya and Ovacik fault zones: Turkish Journal of Earth Sciences, v. 15, p. 123–154.

Kendrick, M.A., Miller, J. McL., and Phillips, D., 2006, Part II. Evaluation of ^{40}Ar-^{39}Ar quartz ages: Implications for fluid inclusion retentivity and determination of initial ^{40}Ar/^{36}Ar values in Proterozoic samples: Geochimica et Cosmochimica Acta, v. 70, p. 2562–2576.

Köksal, S., Romer, R.L., Göncüoğlu, M.C., and Toksoy-Köksal, F., 2004, Timing of post-collisional H-type to A-type granitic magmatism: U-Pb titanite ages from the Alpine central Anatolian granitoids (Turkey): International Journal of Earth Sciences, v. 93, p. 974–989, DOI 10.1007/s00531-004-0432-5.

Košler, J., Forst, L., and Sláma, J., 2008, Lamdate and Lamtool: Spreadsheet-based data reduction for laser ablation ICP-MS: Mineralogical Association of Canada Short Course Series, Short Course 40, p. 315–317.

Kusakabe, M., and Robinson, B.W., 1977, Oxygen and sulfur isotope equilibria in the $BaSO_4$-HSO_4-H_2O system from 110 to 350°C and applications: Geochimica et Cosmochimica Acta, v. 41, p. 1033–1040.

Kuşcu, İ., Yılmazer, E., and Demirela, G., 2002, Sivas-Divriği Bölgesi skarn tipi Demir Oksit yataklarına Fe-oksit-Cu-Au (Olympic Dam tipi) perspektifinden yeni bir bakış: Türkiye Jeoloji Kurumu Bülteni, v. 45, p. 33–47.

Kuşcu, İ., Yılmazer, E., Demirela, G., and Gökçe, H., 2005, Fe-oxide-Cu-Au potential of some "skarn-type" Fe-oxide deposits in central and western Anatolia: Geology, Mining and Current Problems of Turkish Iron Deposits Conference, Proceedings, p. 181–206 (in Turkish with English abs.).

Kuşcu, İ., Gençalioğlu-Kuşcu, G., and Tosdal, R.M., 2007a, Tectonomagmatic-metallogenic framework of mineralization events in the southern NeoTethyan arc, southeastern Turkey: Biennial SGA Meeting, 9th, Mineral Exploration and Research: Digging Deeper, Dublin, Proceedings, p. 1347–1350.

Kuşcu, İ., Yılmazer, E., and Demirela, G., 2007b, Iron oxide-copper ± gold deposits in Turkish Tethyan collage: Biennial SGA Meeting, 9th, Mineral Exploration and Research: Digging Deeper, Dublin, Proceedings, p. 853–857.

Kuşcu, İ., Yılmazer, E, Demirela, G., N Güleç, Kuşcu, G., Kaymakcı, N., Gökçe, H., Şalış, B., and Marschik, R., 2007c, Hasançelebi-Hekimhan (Malatya) Bölgeleri Demiroksit Yataklarının Demir Oksit-Bakır-Altın (DOBA) Yatakları Açısından İncelenmesi ve Bakır-Altın Potansiyellerinin Araştırılması: TÜBİTAK Project-ÇAYDAG 103Y023, 190 (in Turkish with English abs.).

Kuşcu, İ., Gençalioğlu-Kuşcu, Tosdal, R.M., Ullrich, T., and Friedman, R., 2007d, Link between magmatism and subduction-related events in eastern-southeastern Turkey: Geophysical Research Abstracts, v. 9, 04814, 2007 SRef-ID: 1607-7962/gra/EGU2007-A-04814.

Kuşcu, İ., Gençalioğlu-Kuşcu, G., Tosdal, R.M., Ullrich, T., and Friedman, R., 2010, Magmatism in the southeastern Anatolian orogenic belt: Transition from arc to post-collisional setting in an evolving orogen: Geological Society of London Special Publication 340, p. 437–460.

Le Roux, A.P., 1986, Geochemical correlation between southern African kimberlites and south Atlantic hotspots: Nature, v. 324, p. 243– 245.

Leo, G.W., Marvin, R.F., and Mehnert, H.H., 1973, Potassium-argon ages of igneous rocks in the Kulunçak-Sofular area, Malatya province, central Turkey: Ankara, Turkey, General Directorate of Mineral Research and Exploration (MTA), Internal Report, 16 p.

Ludwig, K.R., 2003, Isoplot 3.09. A geochronological toolkit for Microsoft Excel: Berkeley Geochronology Center Special Publication 4.

Mark, G., Foster, D.R.W., Pollard, P.J., Williams, P.J., Tolman, J., Darvall, M., and Blake, K.L., 2004a, Stable isotope evidence for magmatic fluid input during large-scale Na-Ca alteration in the Cloncurry Fe oxide Cu-Au district, NW Queensland, Australia: Terra Nova, v. 16, p. 54–61.

Mark, G., Mustard, R., Foster, D.R.W., and Pollard, P.J., 2004b, Sr-Nd isotopic insights into the evolution of the Cloncurry district, Mount Isa inlier: Predictive Mineral Discovery, Cooperative Research Centre (CRC) Conference, Barossa Valley, 1–3 June, 2004, p. 127–131.

Mark, G., Oliver, N.H.S., and Williams, P.J., 2006, Mineralogical and chemical evolution of the Ernest Henry Fe oxide-Cu-Au ore system, Cloncurry district, northwest Queensland, Australia: Mineralium Deposita, v. 40, p. 769–801.

Marschik, R., Spikings, R., and Kuşcu, İ., 2008, Geochronology and stable isotope signature of alteration related to hydrothermal magnetite ores in Central Anatolia, Turkey: Mineralium Deposita, v. 43, p. 111–124.

Martinsson, O., 1997, Paleoproterozoic greenstones at Kiruna in northern Sweden: A product of continental rifting and associated mafic ultramafic volcanism: Unpublished Ph.D.thesis, Luleå University of Technology, 19, Paper 1, 49 p.

Meinert, L.D., Hedenquist, J.W., Satoh, H., and Matsuhisa, Y., 2003, Formation of anhydrous and hydrous skarn in Cu-Au ore deposits by magmatic fluids: Economic Geology, v. 98, p. 147–156.

Meyer, F.M., Kolb, J., Sakellaris, G.A., and Gerdes, A., 2006, New ages from the Mauritanides belt: Recognition of Archean IOCG mineralization at Guelb Moghrein, Mauritania: Terra Nova, v. 18, p. 345–352.

Monteiro, L.V.S., Xavier, R.P. , de Carvalho, E.R., Hitzman, M.W., Johnson C.A., de Souza Filho, C.R., and Torresi, I., 2006, Spatial and temporal zoning of hydrothermal alteration and mineralization in the Sossego iron oxide-copper-gold deposit, Carajás mineral province, Brazil: Paragenesis and stable isotope constraints: Mineralium Deposita, DOI 10.1007/s00126-006-0121-3.

Niiranen, T., Poutiainen, M., and Manttari, I., 2007, Geology, geochemistry, fluid inclusion characteristics, and U-Pb age studies on iron oxide-Cu-Au deposits in the Kolari region, northern Finland: Ore Geology Reviews, v. 30, p. 75–105.

O'Nions, R.K., Hamilton, P.J., and Evensen, N.M., 1977, Variations in ^{143}Nd/^{144}Nd and ^{87}Sr/^{86}Sr ratios in oceanic basalts: Earth and Planetary Science Letters, v. 34, p. 13–22.

Özgül, N., Turkuca, A., Ozyardımcı, N., Bingol, I., Senol, M., and Uysal, S., 1981, Munzurların temel jeoloji özellikleri: Ankara, Turkey, General Directorate of Mineral Research and Exploration (MTA), Internal Report 6995 (in Turkish with English abs.).

Parlak, O., Hock, V, Kozlu, H., and Delaloye, M., 2004, Oceanic crust generation in an island arc tectonic setting, SE Anatolian orogenic belt (Turkey): Geological Magazine, v. 141, p. 583–603.

Pearce, J.A., 1983. Role of subcontinental lithosphere in magma genesis at active continental margins, *in* Hawkesworth, C.J., and Norry, M.J., eds., Continental basalts and mantle xenoliths: Nantwich, Cheshire, Shiva, p. 230–249.

——1996, A user's guide to basalt discrimination diagrams: Geological Association of Canada Short Course Notes, v. 12, p. 79–113.

Pearce, J.A., Harris, N.B.W., and Tindle, A.G., 1984, Trace element discrimination diagrams for the tectonic interpretation of granitic rocks: Journal of Petrology, v. 25, p. 956–983.

Perinçek, D., and Kozlu, H., 1984, Stratigraphical and structural relations of the units in the Afsin-Elbistan-Doganselhir region (eastern Taurus): International Symposium, Ankara, Turkey, General Directorate of Mineral Research and Exploration (MTA), Proceedings, p. 181–198.

Perring, C.S., Pollard, P. J, Dong, G., Nunn, A.J., and Blake, K.L., 2000, The Lightning Creek sill complex, Cloncurry district, northwest Queensland: A source of fluid for Fe-oxide-Cu-Au mineralization and sodic–calcic alteration: Economic Geology, v. 95, p. 1067–1069.

Pilz, P., 1937, Eisenvorkomen wistlich und istlich-von Hasançelebi bei Deveci, Karakuztepe und Çaltepe Unveröff. Berlin: Ankara, Turkey, General Directorate of Mineral Research and Exploration (MTA), Archive, 30 p.

Pollard, P.J., 2001, Sodic-(calcic) alteration in Fe-oxide-Cu-Au districts: An origin via unmixing of magmatic H_2O-CO_2-NaCl ± $CaCl_2$-KCl fluids: Mineralium Deposita, v. 36, p. 93–100.

Pollard, P. J., 2006, An intrusion-related origin for Cu-Au mineralization in iron oxide-copper-gold (IOCG) provinces: Mineralium Deposita, v. 41, p. 179–187.

Pretorius, W., Weis D., Williams G., Hanano D., Kieffer B., and Scoates J.S. 2006, Complete trace elemental characterization of granitoid (USGSG-2,GSP-2) reference materials by high resolution inductively coupled plasma-mass spectrometry: Geostandards and Geoanalytical Research, v. 30, p. 39–54.

Renne, P.R., C.Swisher, C.C., III, Deino, A.L., Karner, D.B., Owens, T., and DePaolo, D.J., 1998, Intercalibration of standards, absolute ages and uncertainties in ^{40}Ar/^{39}Ar dating: Chemical Geology, v. 145, p. 117–152.

Robertson, A.H.F., 1998, Mesozoic-Cenozoic tectonic evolution of the easternmost Mediterranean area: Integration of marine and land evidence, *in* Robertson, A.H.F., Emeis, K.-C., and Camerlenghi, A., eds., Proceedings of the Ocean Drilling Program, Scientific Results, p. 723–782.

Robertson, A.H.F., and Woodcock, N.H., 1982, Sedimentary history of the south-western segment of the Mesozoic-Cenozoic Antalya continental margin, south-western Turkey: Eclogae Geologicae Helvetiae, v. 75, p. 517–562.

Robertson, A.H.F., Ustaomer, T., Parlak, O., Unlugenc, U.C., Tasl, K., and Inan, N., 2005, Late Cretaceous-Early Tertiary tectonic evolution of south-Neotethys in SE Turkey: Evidence from the Tauride thrust belt in SE Turkey (Binboga-Engizek segment): Journal of Asian Earth Sciences, doi:10.1016/j.jseaes.2005.02.004.

Rollinson, H.R., 1993, Using geochemical data: Evaluation, presentation, interpretation: Essex, Longman, 352 p.

Schimidberger, S.S., and Hegner, E., 1999, Geochemistry and isotope systematics of calc-alkaline volcanic rocks from the Saar-Nahe basin (SW-Germany)—implications for Late Variscan orogenic development: Contributions to Mineralogy and Petrology, v. 135, p. 373–385.

Scrivner, A.E., Vance, D., and Rohling, E.J., 2004, New neodymium isotope data quantify Nile involvement in Mediterranean anoxic episodes: Geology, v. 32, p. 565–568.

Şengör, A.M.C., and Yılmaz, Y., 1981, Tethyan evolution of Turkey: A plate tectonic approach: Tectonophysics, v. 75, p. 181–241.

Sezerer-Kuru, G., Kuşcu, İ., Şalış B., Yılmazer, E., and Demirela, G., 2006, Hasançelebi (Malatya) demir oksit yataklarının oluşum koşulları: mikrotermometrik bir yaklaşım: Ankara, Turkey, General Directorate of Mineral Research and Exploration (MTA), Bulletin, v. 132, p. 101–111.

Sheppard, S.M.F., 1986, Characterization and isotopic variations in natural waters: Reviews in Mineralogy, p. 165– 185.

Shmulovich, K.I., Landwehr, D., Simon, K., and Heinrich, W., 1999, Stable isotope fractionation between liquid and vapour in water-salt systems up to 600°C: Chemical Geology, v. 157, p. 343–354.

Sillitoe, R., 2003, Iron oxide-copper-gold deposits: An Andean view: Mineralium Deposita, v. 38, p. 787–812.

Skirrow, R.G., 1999, Proterozoic Cu-Au-Fe mineral systems in Australia: Filtering key components in exploration models, *in* Stanley, C.J. et al., eds., Mineral deposits: Processes to processing: Rotterdam, A.A. Balkema, p. 1361–1364.

——2000, Gold-copper-bismuth deposits of the Tennant Creek district, Australia: A reappraisal of diverse high grade systems, *in* Porter, T.M., ed., Hydrothermal iron oxide copper-gold and related deposits: A global perspective: Australian Mineral Foundation, p. 149–160.

Skirrow, R.G., Bastrakov, E., Davidson, G.J., Raymond, O., and Heithersay, P., 2002, Geological framework, distribution and controls of Fe-oxide Cu-Au deposits in the Gawler craton. Part II. Alteration and mineralization, *in* Porter, T.M., ed., Hydrothermal iron oxide copper-gold and related deposits: Adelaide, South Australia, Porter GeoConsultancy Publishing, v. 2, p. 33–47.

Skirrow, R.G., Bastrakov, E.N., Barovich, K., Fraser, G.L., Creaser, R.A., Fanning, C.M., Raymond, O.L., and Davidson, G.J., 2007, Timing of iron oxide Cu-Au-(U) hydrothermal activity and Nd isotope constraints on metal sources in the Gawler craton, South Australia: Economic Geology, v. 102, p. 1441–1470.

Spivack, A.J., and Wasserburg, G.J., 1988, Neodymium isotopic composition of the Mediterranean outflow and the eastern North Atlantic: Geochimica Cosmochimica Acta, v. 52, p. 2767–2773.

Stampfli, G.M., 2001, Tethyan oceans, *in* Bozkurt, E., Winchester, J.A., and Piper, J.D.A., eds., Tectonics and magmatism in Turkey and the surrounding area: Geological Society London Special Publication 173, p. 1–23.

Stampfli, G., Mosar, J., Bono, A de, and Vavasis, I., 1998, Late Paleozoic, early Mesozoic plate tectonics of the western Tethys: Bulletin of Geological Society of Greece, v. 32, p. 113–120.

Steiger, R.H., and Jager, E., 1977, Subcomission on geochronology: Convention on the use of decay constants in geo- and cosmochronology: Earth and Planetary Science Letters, v. 36, p. 359–362.

Stendal, H., Ünlü, T., and Konnerup-Madsen, J., 1995, Geological setting of iron deposits of Hekimhan province, Malatya, Central Anatolia, Turkey: Transactions of the Institution of Mining and Mineralization, v. 104, p. B46–B54.

Sun, S.S., and McDonough, W.F., 1989, Chemical and isotopic systematics of oceanic basalts: Implications for mantle composition and processes: Geological Society of London Special Publication 42, p. 313–345.

Suzuoki, T., and Epstein, S., 1976, Hydrogen isotope fractionation between OH-bearing minerals and water: Geochimica et Cosmochimica Acta, v. 40, p. 1129–1240.

Taylor, B.E., 1986, Magmatic volatiles: Isotopic variation of C, H and S: Reviews in Mineralogy, v. 16, p. 185–226.

——1988, Degassing of rhyolitic magmas: Hydrogen isotope evidence and implications for magmatic hydrothermal ore deposits: Canadian Institute of Mining and Metallurgy Special Publication 39, p. 33–49.

——1992, Degassing of H_2O from rhyolitic magma during eruption and shallow intrusion, and the isotopic composition of magmatic water in hydrothermal systems: Geological Survey of Japan Report 279, p. 190–194.

Taylor, H.P., Jr., 1997, Oxygen and hydrogen isotope relationships in hydrothermal mineral deposits, *in* Barnes, H.L., ed., Geochemistry of hydrothermal ore deposits, 3rd ed.: New York, Wiley, p. 229–302.

Uçurum, A., Larson, L.T., and Boztuğ, D., 1996, Geology, geochemistry, and petrology of the alkaline subvolcanic trachyte-hosted iron deposit in the Karakuz area, northwestern Hekimhan-Malatya, Turkey: International Geology Review, v. 38, p. 995–1005.

Ünlü, T., Stendal, H., Makovicky, E., and Sayılı, S., 1995, Genesis of the Divriği iron ore deposit, Sivas, central Anatolia, Turkey: An ore microscopy study: Bulletin of Mineral Research and Exploration Institute of Turkey, v. 117, p. 17–28.

Wang, Y., Fan, W., Peng, T., Zhang, H., and Guo, F., 2005, Nature of the Mesozoic lithospheric mantle and tectonic decoupling beneath the Dabie orogen, central China: Evidence from $^{40}Ar/^{39}Ar$ geochronology, elemental and Sr-Nd-Pb isotopic compositions of Early Cretaceous mafic igneous rocks: Chemical Geology, v. 220, p. 165–189.

Wapstra, A.H., and Bos, K., 1977, Atomic mass evaluation: Atomic Data and Nuclear Data Tables, v. 19, p. 175.

Wasserburg, G.J., Jacobsen, S.B., De Paolo, D.J., Mc Culloch, M.T., and Wen, T., 1981, Precise determination of Sm/Nd ratios, Sm and Nd isotopic abundances in standard solutions: Geochimica et Cosmochimica Acta, v. 45, p. 2311–2323.

Weis, D., Kieffer B., Hanano D., Nobre Silva I., Barling J., Pretorius W., Maerschalk C., and Mattielli N.2007, Hf isotope compositions of U.S.Geological Survey reference materials: Geochem Geophys.Geosyst., v. 8, Q06006, doi:10.1029/2006GC001473.

Whalen, J.B., Currie, K.L., and Chappel, B.W., 1987, A-type granites: Geochemical characteristics, discrimination and petrogenesis: Contributions to Mineralogy and Petrology, v. 95, p. 407–419.

Williams P.J., Barton, M.D., Johnson, D.A., Fontboté, L., de Haller A., Mark, G., Oliver, N.H.S., and Marschik, R., 2005, Iron oxide-copper-gold deposits: Geology, space-time distribution, and possible modes of origin: Economic Geology 100th Anniversary Volume, p. 371–405.

Winchester, J.A., and Floyd, P.A., 1977, Geochemical discrimination of different magma series and their differentiation products using immobile elements: Chemical Geology, v. 20, p. 325–343.

Yalçın, H., Gündoğdu, M.N., Gourgaud, A., Vidal, P., and Uçurum, A., 1998, Geochemical characteristics of Yamadağı Volcanics in central east Anatolia: An example from collision-zone volcanism: Journal of Volcanology and Geothermal Research, v. 85, p. 303–326.

Yalınız, M.K., Aydın, N.S., Göncüoğlu, M.C., and Parlak,O., 1999, Terlemez quartz monzonite of central Anatolia (Aksaray-Sarıkaraman): Age, petrogenesis and geotectonic implications for ophiolite emplacement: Geological Journal, v. 34, p. 233–242.

Yıldız, A., and Özdemir, Z., 1999, Biostratigraphic and isotopic data on the Coreklik Member of the Hekimhan Formation (Campanian-Maastrichtian) of SE Turkey and their palaeoenvironmental significance: Cretaceous Research, v. 20, p. 107–117.

Yılmaz, S., Boztuğ, D., and Öztürk, A., 1993, Geological setting, petrographic and geochemical characteristics of the Cretaceous and Tertiary igneous rocks in the Hekimhan-Hasançelebi area, northwest Malatya, Turkey: Geological Journal, v. 28, p. 383–398.

Yılmaz, Y., Yiğitbaş, E., and Yıldırım, M., 1987, Güneydoğu Anadolu'da Triyas sonu tektonizması ve bunun jeolojik anlamı: Türkiye Petrol Jeologları Derneği Türkiye 7. Petrol Kongresi Bildirileri, p. 65–77 (in Turkish with English abs.).

Yılmazer, E., Kuşcu, İ., and Demirela, G., 2003, Divriği A-B kafa cevherleşmeleri: alterasyon zonları ve zonlanma süreçleri: Türkiye Jeoloji Bulletin, v. 46, p. 17–34 (in Turkish with English abs.).

Yüce, A.E., Güney, A., Elevli, B., Kökkılıç, O., Acarkan.N., Önal, G., and Demirci, A., 2005, Hasançelebi yatağı revize fizibilitesi: Sponsored by Istanbul University, Chamber of Geological Engineers and Mining Engineers, and Scientific and Technical Research Council of Turkey, Geology, Mining and Current Problems of Turkish Iron Deposits Conference, Proceedings, p. 306–319 (in Turkish with English abs.).

Zheng, Y.F., 1993a, Calculation of oxygen isotope fractionation in hydroxyl-bearing silicates: Earth and Planetary Science Letters, v. 120, p. 247–263.

——1993b, Calculation of oxygen isotope fractionation in anhydrous silicate minerals: Geochimica et Cosmochimica Acta, v. 57, p. 1079–1091.

APPENDIX 1

A. Results of $^{40}Ar/^{39}Ar$ Analyses (the uncertainties are 2σ)

Sample 321, Syenite = K-feldspar — Coordinates (UTM, Datum European 1950: 403110–4309055)

Laser	Isotope ratios									
	$^{40}Ar/^{39}Ar$	$^{38}Ar/^{39}Ar$	$^{37}Ar/^{39}Ar$	$^{36}Ar/^{39}Ar$	Ca/K	Cl/K	$\%^{40}Ar$ atm	$f^{39}Ar$	$^{40}Ar^*/^{39}ArK$	Age
2	47.621 ± 0.007	0.300 ± 0.027	0.075 ± 0.030	0.151 ± 0.020	0.32	0.059	93.64	1.72	2.978 ± 0.878	54.41 ± 15.80
2.2	11.009 0.005	0.080 0.023	0.077 0.021	0.024 0.023	0.393	0.014	64.19	5.59	3.872 0.163	70.45 2.91
2.4	6.490 0.005	0.034 0.043	0.055 0.024	0.008 0.028	0.28	0.004	37.13	7.29	3.998 0.073	72.69 1.30
2.6	5.917 0.005	0.025 0.032	0.048 0.025	0.007 0.036	0.239	0.002	31.63	6.32	3.950 0.074	71.84 1.32
2.8	4.679 0.004	0.027 0.016	0.016 0.029	0.002 0.040	0.083	0.003	14.01	28.36	3.972 0.032	72.22 0.57
3	5.273 0.004	0.036 0.019	0.037 0.017	0.004 0.023	0.193	0.005	24.46	20.01	3.927 0.035	71.43 0.62
3.2	6.769 0.005	0.054 0.019	0.081 0.022	0.010 0.028	0.415	0.009	40.46	5.87	3.939 0.082	71.65 1.45
3.4	5.737 0.005	0.046 0.027	0.033 0.045	0.006 0.045	0.151	0.007	29.11	4.7	3.948 0.083	71.79 1.49
3.7	5.899 0.004	0.042 0.018	0.091 0.016	0.007 0.019	0.492	0.006	32.32	12.63	3.928 0.043	71.45 0.76
4	5.682 0.005	0.042 0.032	0.054 0.024	0.006 0.041	0.281	0.006	28.27	7.51	3.988 0.071	72.51 1.27
Total/average	6.440 ± 0.001	0.042 ± 0.004	0.131 ± 0.002	0.008 ± 0.005		0.011		100	3.933 ± 0.013	

J = 0.010284 ± 0.000012

Sample 323, Diabase: Hornblende — Coordinates (UTM, Datum European 1950: 403456–4309467)

Laser	Isotope ratios									
Power (%)	$^{40}Ar/^{39}Ar$	$^{38}Ar/^{39}Ar$	$^{37}Ar/^{39}Ar$	$^{36}Ar/^{39}Ar$	Ca/K	Cl/K	$\%^{40}Ar$ atm	$f^{39}Ar$	$^{40}Ar^*/^{39}ArK$	Age
2	60.679 ± 0.007	0.190 ± 0.034	0.486 ± 0.025	0.190 ± 0.021	1.961	0.032	93.03	1.97	4.173 ± 1.120	39.68 ± 10.53
2.3	29.946 0.005	0.199 0.020	0.692 0.014	0.073 0.020	2.79	0.039	71.89	6.49	8.355 0.427	78.58 3.93
2.4	13.855 0.008	0.333 0.016	1.352 0.016	0.020 0.035	5.397	0.073	40.87	6.07	8.094 0.222	76.17 2.05
2.8	11.065 0.006	0.495 0.012	1.104 0.014	0.011 0.029	4.404	0.111	28.04	11.92	7.890 0.110	74.29 1.02
3.1	9.447 0.007	1.091 0.012	0.691 0.015	0.005 0.049	2.755	0.248	14.29	16.85	8.027 0.095	75.55 0.88
3.4	8.918 0.004	2.062 0.009	0.374 0.013	0.004 0.052	1.492	0.472	10.84	20.67	7.884 0.068	74.23 0.62
3.7	8.827 0.007	2.904 0.010	0.473 0.016	0.004 0.071	1.887	0.666	9.72	13.84	7.885 0.095	74.24 0.87
4	8.780 0.005	4.810 0.009	0.908 0.013	0.004 0.053	3.622	1.107	9.5	14.34	7.868 0.072	74.09 0.66
4.6	8.920 0.007	5.159 0.011	1.115 0.015	0.005 0.078	4.45	1.187	12.79	7.85	7.666 0.129	72.22 1.19
Total/average	11.834 ± 0.001	2.204 ± 0.002	1.623 ± 0.001	0.014 ± 0.006		0.437		100	7.666 ± 0.026	

J = 0.005328 ± 0.000006

Sample 331, Trachyte: Biotite — Coordinates (UTM, Datum European 1950: 400382–4311027)

Laser	Isotope ratios									
Power(%)	$^{40}Ar/^{39}Ar$	$^{38}Ar/^{39}Ar$	$^{37}Ar/^{39}Ar$	$^{36}Ar/^{39}Ar$	Ca/K	Cl/K	$\%^{40}Ar$ atm	$f^{39}Ar$	$^{40}Ar^*/^{39}ArK$	Age
2	143.587 ± 0.007	0.305 ± 0.026	0.158 ± 0.039	0.488 ± 0.020	0.727	0.045	100.49	0.57	−0.729 ± 2.814	13.57 ± 52.5
2.2	16.371 0.013	0.159 0.024	0.159 0.025	0.050 0.028	0.83	0.031	89.01	1.6	1.746 0.426	32.07 7.76
2.4	8.789 0.010	0.128 0.022	0.034 0.021	0.018 0.022	0.179	0.025	58.95	7.09	3.555 0.125	64.73 2.23
2.6	5.700 0.013	0.121 0.020	0.010 0.032	0.005 0.035	0.049	0.024	27.68	10.88	4.067 0.082	73.85 1.45
2.8	4.835 0.020	0.130 0.025	0.009 0.031	0.002 0.030	0.044	0.027	11.96	19.34	4.207 0.090	76.35 1.61
3	4.664 0.011	0.149 0.018	0.012 0.037	0.001 0.035	0.064	0.031	7.32	15.19	4.268 0.051	77.43 0.90
3.2	4.604 0.017	0.173 0.021	0.026 0.031	0.001 0.053	0.138	0.037	6.98	14.06	4.227 0.076	76.70 1.35
3.4	4.502 0.012	0.196 0.017	0.039 0.019	0.001 0.045	0.209	0.042	5.15	12.07	4.211 0.054	76.41 0.95
3.6	4.476 0.012	0.232 0.017	0.060 0.020	0.001 0.088	0.323	0.05	5.79	7.47	4.143 0.061	75.20 1.09
3.9	4.401 0.013	0.015	0.098 0.021	0.001 0.092	0.535	0.047	4.8	8.36	4.120 0.060	74.80 1.07
4.4	4.524 0.017	0.270 0.020	0.258 0.021	0.002 0.149	1.404	0.059	5.86	3.37	4.138 0.102	75.11 1.81
Total/ Average	5.972 ± 0.003	0.167 ± 0.004	0.117 ± 0.002	0.006 ± 0.006		0.038		100	4.076 ± 0.017	

J = 0.010275 ± 0.000012

APPENDIX *(Cont.)*

Sample 336, Leylekda , Trachyte: K-feldspar — Coordinates (UTM, Datum European 1950: 394224–4305713)

Laser	Isotope ratios									
Power (%)	$^{40}Ar/^{39}Ar$	$^{38}Ar/^{39}Ar$	$^{37}Ar/^{39}Ar$	$^{36}Ar/^{39}Ar$	Ca/K	Cl/K	%^{40}Ar atm	$f\,^{39}$Ar	$^{40}Ar^*/^{39}ArK$	Age
2.00	22.852 ± 0.008	0.029 ± 0.030	0.129 ± 0.029	0.066 ± 0.021	0.373	0.001	85.89	14.50	3.178 ± 0.414	30.29 ± 3.91
2.20	15.304 0.006	0.023 0.072	0.203 0.016	0.040 0.023	0.588	0.000	76.83	10.97	3.482 0.271	33.17 2.56
2.40	11.623 0.008	0.021 0.075	0.283 0.027	0.028 0.024	0.820	0.000	69.59	14.08	3.470 0.190	33.06 1.80
2.60	10.496 0.005	0.020 0.071	0.395 0.023	0.022 0.050	1.146	0.000	62.20	8.20	3.868 0.329	36.81 3.10
2.80	10.551 0.006	0.024 0.101	0.418 0.018	0.023 0.039	1.211	0.001	64.13	7.49	3.682 0.264	35.06 2.49
3.10	32.626 0.005	0.046 0.047	0.646 0.015	0.097 0.021	1.876	0.003	88.09	10.13	3.838 0.604	36.53 5.69
3.40	31.271 0.008	0.047 0.056	0.786 0.021	0.093 0.025	2.282	0.004	87.27	5.63	3.919 0.652	37.29 6.14
3.80	45.415 0.011	0.071 0.039	1.000 0.017	0.142 0.019	2.907	0.007	92.17	10.71	3.515 0.855	33.48 8.07
4.20	37.283 0.005	0.071 0.037	0.802 0.015	0.113 0.023	2.331	0.008	89.82	8.68	3.749 0.773	35.69 7.28
4.60	48.156 0.007	0.081 0.051	1.245 0.017	0.149 0.020	3.621	0.009	91.48	7.45	4.061 0.830	38.63 7.81
5.00	63.384 0.008	0.089 0.080	1.051 0.020	0.203 0.024	3.052	0.008	94.60	2.15	3.360 1.378	32.02 13.01
Total/ Average	26.224 ± 0.001	0.042 ± 0.008	0.866 ± 0.002	0.077 ± 0.004		0.004		100.00	3.831 ± 0.093	

J = 0.005329 ± 0.000006

Sample 328, Preore K-Fe alteration ((early) phlogopite), biotite — Coordinates (UTM, Datum European 1950: 402801–4310545)

Laser	Isotope ratios									
Power (%)	$^{40}Ar/^{39}Ar$	$^{38}Ar/^{39}Ar$	$^{37}Ar/^{39}Ar$	$^{36}Ar/^{39}Ar$	Ca/K	Cl/K	%^{40}Ar atm	$f\,^{39}$Ar	$^{40}Ar^*/^{39}ArK$	Age
2	728.369 ± 0.008	0.590 ± 0.030	0.093 ± 0.087	2.534 ± 0.018	0,395	0,022	103,11	0,12	−22.603 ± 12.117	−476.37 ± 292.2
2,2	52.538 0.013	0.163 0.033	0.190 0.031	0.171 0.021	1,027	0,027	96,52	0,35	1.779 0.995	32.66 18.10
2,4	29.079 0.008	0.140 0.021	0.482 0.021	0.092 0.020	2,699	0,025	93,29	0,57	1.898 0.533	34.82 9.68
2,6	22.278 0.005	0.120 0.017	0.188 0.017	0.064 0.022	1,057	0,022	84,81	1,2	3.328 0.422	60.61 7.56
2,8	11.439 0.005	0.116 0.013	0.011 0.039	0.026 0.019	0,055	0,022	66,92	3,36	3.732 0.148	67.83 2.63
3	6.401 0.004	0.114 0.013	0.002 0.096	0.008 0.022	0,006	0,023	35,25	6,68	4.092 0.054	74.24 0.97
3,2	5.056 0.004	0.113 0.013	0.001 0.039	0.003 0.026	0,004	0,023	16,31	9,35	4.180 0.028	75.81 0.50
3,4	4.772 0.006	0.115 0.010	0.001 0.068	0.002 0.027	0,004	0,023	11,5	11,76	4.174 0.029	75.71 0.51
3,6	4.513 0.007	0.116 0.012	0.001 0.066	0.001 0.050	0,004	0,023	6,72	11,19	4.160 0.033	75.45 0.59
3,8	4.411 0.005	0.116 0.011	0.001 0.059	0.001 0.028	0,005	0,023	5,89	13,94	4.104 0.023	74.45 0.42
4	4.374 0.005	0.115 0.010	0.001 0.062	0.001 0.036	0,005	0,023	5,22	12,76	4.097 0.021	74.34 0.38
4,4	4.336 0.005	0.116 0.010	0.001 0.030	0.001 0.042	0,003	0,023	4,6	15,52	4.091 0.023	74.22 0.40
4,8	4.326 0.005	0.114 0.011	0.001 0.099	0.001 0.045	0,003	0,023	4,24	13,2	4.095 0.023	74.30 0.40
Total/average	6.232 ± 0.001	0.116 ± 0.002	0.021 ± 0.002	0.007 ± 0.004		0,023		100	4.107 ± 0.011	

J = 0.010267 ± 0.000012

Sample 327, Synore K-Fe alteration: K-feldspar — Coordinates (UTM, Datum European 1950: 402807–4310543)

Laser	Isotope ratios									
Power(%)	$^{40}Ar/^{39}Ar$	$^{38}Ar/^{39}Ar$	$^{37}Ar/^{39}Ar$	$^{36}Ar/^{39}Ar$	Ca/K	Cl/K	%^{40}Ar atm	$f\,^{39}$Ar	$^{40}Ar^*/^{39}ArK$	Age
2	30.004 ± 0.004	0.658 ± 0.010	0.395 ± 0.017	0.100 ± 0.018	2.1	0.144	98.37	4.42	0.456 ± 0.536	8.41 ± 9.88
2.2	5.996 0.005	0.696 0.013	0.058 0.034	0.008 0.027	0.3	0.157	37.25	4.58	3.608 0.068	65.60 1.22
2.4	4.669 0.005	0.906 0.011	0.032 0.036	0.003 0.065	0.163	0.205	13.89	6.43	3.868 0.058	70.23 1.03
2.6	4.336 0.004	2.007 0.009	0.039 0.027	0.002 0.092	0.207	0.459	7.43	9.31	3.893 0.050	70.67 0.89
2.8	4.054 0.004	2.641 0.009	0.052 0.019	0.001 0.097	0.275	0.605	4.08	10.66	3.776 0.039	68.59 0.69
3	4.045 0.004	1.564 0.009	0.038 0.016	0.001 0.040	0.203	0.357	5.05	24.23	3.772 0.020	68.51 0.36
3.2	4.121 0.004	2.797 0.009	0.082 0.014	0.001 0.039	0.438	0.641	6.39	24.98	3.791 0.023	68.86 0.41
3.4	4.110 0.004	2.439 0.009	0.079 0.019	0.001 0.130	0.416	0.559	4.82	7.53	3.768 0.059	68.44 1.05
3.7	4.233 0.004	0.057 0.024	0.005 0.052	0.001 0.128	0.024	0.01	3.14	7.86	3.958 0.039	71.82 0.70
Total/ Average	5.303 ± 0.001	1.854 ± 0.002	0.195 ± 0.001	0.006 ± 0.008		0.349		100	3.779 ± 0.014	

J = 0.010262 ± 0.000012

APPENDIX *(Cont.)*

Sample 318a, Synore K-Fe alteration: K-feldspar — Coordinates (UTM, Datum European 1950: 402652–4309770)

Laser	Isotope ratios									
	$^{40}Ar/^{39}Ar$	$^{38}Ar/^{39}Ar$	$^{37}Ar/^{39}Ar$	$^{36}Ar/^{39}Ar$	Ca/K	Cl/K	%^{40}Ar atm	$f\,^{39}$Ar	$^{40}Ar^{*}/^{39}ArK$	Age
2	105.570 ± 0.008	1.484 ± 0.018	0.158 ± 0.071	0.357 ± 0.021	0,509	0,326	99,27	0,29	0.742 ± 2.041	13.06 ± 35.82
2,2	17.182 0.005	0.303 0.021	0.116 0.037	0.047 0.028	0,454	0,065	79,02	1,51	3.527 0.385	61.29 6.57
2,4	8.275 0.004	0.101 0.014	0.136 0.021	0.014 0.023	0,558	0,019	49,32	4,3	4.121 0.099	71.40 1.68
2,6	6.853 0.004	0.069 0.016	0.042 0.020	0.009 0.026	0,168	0,012	38,49	5,1	4.140 0.073	71.74 1.25
2,8	5.188 0.004	0.069 0.020	0.027 0.048	0.003 0.047	0,102	0,012	16,85	4,59	4.216 0.051	73.02 0.86
3,1	5.298 0.004	0.070 0.012	0.023 0.029	0.004 0.040	0,093	0,013	20,89	9,37	4.128 0.050	71.52 0.85
3,4	4.747 0.004	0.058 0.011	0.021 0.027	0.002 0.024	0,087	0,01	13,39	16,95	4.059 0.024	70.36 0.40
3,7	4.865 0.004	0.075 0.011	0.054 0.016	0.003 0.025	0,228	0,014	15,91	25,01	4.045 0.026	70.12 0.45
4	4.826 0.004	0.054 0.011	0.072 0.017	0.002 0.043	0,3	0,009	14,04	12,37	4.090 0.036	70.89 0.62
4,4	5.218 0.004	0.050 0.011	0.082 0.016	0.004 0.026	0,344	0,008	20,89	14,14	4.075 0.035	70.63 0.59
Total/ Average	5.646 ± 0.001	0.072 ± 0.002	0.138 ± 0.002	0.005 ± 0.004		0,045		100	4.080 ± 0.009	

J = 0.009797 ± 0.000010

B. Results of U-Pb Analyses (the uncertainties are 1σ)

Sample 318, Syenite porphyry: Zircon, U-Pb age geochronology — Coordinates (UTM, Datum European 1950: 402651–4309770)

Analysis	$^{207}Pb/^{235}U$	$^{207}Pb/^{235}U$	$^{206}Pb/^{238}U$	$^{206}Pb/^{238}U$	$^{207}Pb/^{206}Pb$	$^{207}Pb/^{206}Pb$	$^{207}Pb/^{235}U$	$^{207}Pb/^{235}U$	$^{206}Pb/^{238}U$	$^{206}Pb^{238}/U$	$^{207}Pb/^{206}Pb$	$^{207}Pb/^{206}Pb$
318T2	0.06928	0.00126	0.01084	0.00006	0.04639	0.00086	68	1.2	69.5	0.38	17.9	43.28
318T3	0.07511	0.00169	0.01117	0.00008	0.04946	0.00113	73.5	1.6	71.6	0.53	169.8	52.6
318T4	0.07497	0.00309	0.01155	0.00017	0.04775	0.00201	73.4	2.92	74	1.06	86	97.78
318T6	0.07576	0.00189	0.01119	0.00009	0.04902	0.00124	74.2	1.78	71.7	0.57	148.8	58.19
318T7	0.07424	0.00148	0.01103	0.00007	0.04846	0.00098	72.7	1.4	70.7	0.44	121.6	46.86
318T9	0.0725	0.00193	0.01114	0.00009	0.04791	0.0013	71.1	1.83	71.4	0.56	93.6	63.94
318T12	0.07176	0.002	0.13939	0.00156	0.05035	0.00144	70.4	1.9	841.2	8.82	211.3	64.95
318T13	0.07473	0.00137	0.02283	0.00015	0.04762	0.00089	73.2	1.3	145.5	0.95	79.6	44.46
318T16	0.07627	0.00144	0.01201	0.00008	0.04956	0.00095	74.6	1.35	77	0.52	174.2	43.99
318T17	0.07426	0.00114	0.07615	0.00044	0.04779	0.00074	72.7	1.08	473.1	2.62	87.8	37.38
318T20	0.07539	0.00048	0.8007	0.0026	0.05424	0.00033	73.8	0.45	3791.6	9.3	380.8	13.78
318T2	0.06928	0.00126	0.01084	0.00006	0.04639	0.00086	68	1.2	69.5	0.38	17.9	43.28
318T3	0.07511	0.00169	0.01117	0.00008	0.04946	0.00113	73.5	1.6	71.6	0.53	169.8	52.6
318T4	0.07497	0.00309	0.01155	0.00017	0.04775	0.00201	73.4	2.92	74	1.06	86	97.78
318T6	0.07576	0.00189	0.01119	0.00009	0.04902	0.00124	74.2	1.78	71.7	0.57	148.8	58.19
318T7	0.07424	0.00148	0.01103	0.00007	0.04846	0.00098	72.7	1.4	70.7	0.44	121.6	46.86
318T9	0.0725	0.00193	0.01114	0.00009	0.04791	0.0013	71.1	1.83	71.4	0.56	93.6	63.94
318T16	0.07627	0.00144	0.01201	0.00008	0.04956	0.00095	74.6	1.35	77	0.52	174.2	43.99
318T3	0.07511	0.00169	0.01117	0.00008	0.04775	0.00113	73.5	1.6	71.6	0.53	169.8	52.6
318T6	0.07576	0.00189	0.01119	0.00009	0.04902	0.00124	74.2	1.78	71.7	0.57	148.8	58.19
318T7	0.07424	0.00148	0.01103	0.00007	0.04846	0.00098	72.7	1.4	70.7	0.44	121.6	46.86
318T9	0.0725	0.00193	0.01114	0.00009	0.04791	0.0013	71.1	1.83	71.4	0.56	93.6	63.94